Title: Epithelial tension controls intestinal cell extrusion

Authors: Daniel Krueger†[1,5]*, Willem Kasper Spoelstra†[2], Dirk Jan Mastebroek[1], Rutger Kok[2,3,6], Shanie Wu[1], Mike Nikolaev[3]‡, Marie Bannier-Hélaouët[1,5]‡, Nikolche Gjorevski [3]‡, Matthias Lutolf[3]‡, Johan van Es[1,5], Jeroen van Zon[2]*, Sander Tans[2,4]*, Hans Clevers[1,5]*§

Affiliations:

[1]Hubrecht Institute, Royal Netherlands Academy of Arts and Sciences (KNAW) and University Medical Centre Utrecht (UMC); Utrecht, the Netherlands.

[2]AMOLF institute; Amsterdam, The Netherlands.

[3]École Polytechnique Fédérale de Lausanne/ Institute of Human Biology; Basel, Switzerland.

[4]Bionanoscience Department, Kavli Institute of Nanoscience Delft, Delft University of Technology; Delft, The Netherlands.

[5]Oncode Institute, Hubrecht Institute; Utrecht, the Netherlands.

†These authors contributed equally

[6]Current address: Center for Molecular Medicine, UMC Utrecht, 3584 CG Utrecht, The Netherlands

‡Current address: Institute of Human Biology (IHB) Roche Pharma Research and Early Development; Basel, Switzerland

§Current address: Pharma, Research and Early Development (pRED) of F. Hoffmann-La Roche Ltd, Basel, Switzerland

*Corresponding authors.

Email: h.clevers@hubrecht.eu; s.tans@amolf.nl; j.v.zon@amolf.nl; d.krueger@hubrecht.eu

Abstract:

Cell extrusion is essential for homeostatic self-renewal of the intestinal epithelium. Cell extrusion is thought to be triggered by crowding-induced compression of cells at the intestinal villus tip. Here we found instead that a local "tug-of-war" competition between contractile cells regulated extrusion in the intestinal epithelium. We combined quantitative live microscopy, optogenetic induction of tissue tension, genetic perturbation of Myosin-II activity, and local disruption of the basal cortex in mouse intestines and intestinal organoids. These approaches revealed that a dynamic actomyosin network generates tension throughout the intestinal villi, including the villus tip region. Mechanically weak cells unable to maintain this tension underwent extrusion. Thus, epithelial barrier integrity depends on intercellular mechanics.

Main Text:

The intestinal epithelium is a defensive barrier protecting the underlying tissue from microbiota, pathogens, and acidity. The turnover of cells within the intestinal epithelium is rapid, and most cells are replaced within a few days (*1*, *2*). Stem cells are generated in the crypt, and then migrate upwards to the tissue protrusions called villi (*3*) as they differentiate and acquire specialized function (*4*, *5*). After several days, mature cells are extruded in a controlled manner into the gut lumen (*6–8*). The mechanisms regulating cell extrusion in the intestine are not well understood (*9*), and current models are largely inferred from non-mammalian model organisms and systems. Apoptotic cell extrusion has been demonstrated to regulate cell numbers in cell lines, *Drosophila* (*10*), and the zebrafish epidermis (*11*, *12*). However, mouse intestines with genetic knockouts of key apoptotic pathway components such as Bcl-2, Bax, Bcl-w, and Caspase-3/7/8 display normal villus morphology, indicating a normal regulation of homeostatic cell extrusion (*13–16*). In Madin-Darby canine kidney (MDCK) monolayers (*17*), zebrafish epidermis (*17*) and the *Drosophila* notum (*18*, *19*), extrusion is driven by increased cell density. These findings have inspired a model for the mammalian intestinal epithelium, in which the flow of cells to the villus causes cell crowding. In that model, compression forces at the villus tip would trigger extrusion (see refs. (*20*) and (*21*) for recent reviews). However, cell extrusion is enriched in – but not limited to – the villus tip: the frequency of cell extrusion gradually increases along the villus shaft, and peaks at the villus tip (*22*, *23*). However, cell density is high in the crypt and at the villus base, lower along the villus shaft, and returns to villus-base levels at the villus tip (*3*). Thus, crowding alone seems insufficient to explain the extrusion pattern.

Previous work suggests that active cell migration along the villus leads to cell crowding at the villus tip, while leaving the villus bottom under tension, as indicated by laser ablation experiments (*3*).

Cell contractility and mechanical forces have been implicated in the regulation of cell extrusion or delamination in other epithelial systems. For example, induction of Rho kinase - an upstream regulator of Myosin II - reduces extrusion in the *Drosophila* notum and zebrafish epidermis (*24–26*). In the *Drosophila* abdominal epidermis, extrusion is associated with pulsatile actomyosin contractions, and extrusion frequency increases under conditions of elevated tensile stress (*27*). In contrast, elevated cortical tension inhibits the apical extrusion of oncogenic H-RasV12 cells in liver epithelial monolayers (*28*). Thus, the role of mechanical force is important for cell extrusion and depends on the tissue context but has remained largely unaddressed in the intestinal villi.

Cells extrude from regions under tension in a crowding-independent manner.

Mouse intestinal organoids faithfully recapitulate the self-renewal processes of the gut epithelium (*6*). At the tips of organoid buds (the equivalents of the Crypts of Lieberkühn), $Lgr5^{+}$ stem cells are interspersed between Paneth cells, the latter serving as a source of niche signals. Daughter cells rapidly proliferate and move away from the buds towards a central villus domain. As they reach the villus domain, the cells differentiate into one of the mature intestinal epithelial cell types, the most abundant being the enterocyte. To establish an experimental platform for mechanistic studies of cell extrusion process, we developed a method to quantify the localization of the cell extrusion events. We imaged mouse intestinal organoids expressing an H2B-mCherry nuclear marker over multiple days. Using a neural network approach (*29*), we tracked single cells and identified hundreds of extruding cells (**Fig. 1A, B & Movie S1**). We observed two distinct extrusion modes: one showed fragmented nuclei prior to extrusion, indicative of extrusion driven by apoptosis; the other showed extrusion with intact nuclei, indicating a live-cell process (**Fig. 1C, D & fig. S1A**). Apoptotic cell extrusion was the predominant form in the stem cell-containing crypt region, where, under physiological in vivo conditions, cell extrusion is typically rare. However, the vast majority

(92%) of extrusions in the villus-like region were live-cell extrusions (**Fig. 1E & fig. S1B**). Next, we tested if cell extrusion was determined by an intrinsic timer set before the last division (*30*). The lifetime of cells – defined as the period between the last division and extrusion – showed major differences for apoptotic and live-cell extrusion. The median lifetime of apoptotic cells was short (6 h) and similar between sister cells: cells had an 82% chance of extruding in apoptotic manner if their sister also did so (**fig. S1C**). Thus, apoptotic cell extrusion appears to result from fatal errors in the mother's cell cycle or during mitosis (*31*). The lifetimes of cells undergoing live-cell extrusion were broadly distributed, with a median of 27 hours (**Fig. 1F & fig. S1D, E**). The lifetime of one sister cell undergoing live-cell extrusion poorly predicted the lifetime of the second sister (**fig. S1F**). Conclusively, live cell extrusion is not controlled by a timer set prior to the cell's birth.

To test whether tissue crowding triggers live-cell extrusion in the intestinal epithelium, we analyzed the positions of extrusion events and the local cell density by tracking nuclei. Nuclei of neighbors of extruding cells initially moved away from the extruding cell and returned directly after extrusion so that the local cell density recovered to pre-extrusion levels within approximately 45 minutes (**fig. S1G, H**). Furthermore, cell extrusion events were spatially and temporally correlated; cells tended to extrude close to each other and shortly after a nearby cell had extruded, typically when cells from different crypts came into contact (**fig. S1I-L**). Notably, extrusions were not concentrated in regions of high cell density. Instead, cells showed a tendency to extrude from areas of average – or low – cell density within the villus-like domain (**Fig. 1G, H**). Thus, cell extrusion in intestinal organoids is not primarily driven by tissue crowding.

These findings prompted us to investigate whether alternative mechanisms involving mechanical forces underlie cell extrusion. We examined the actomyosin network along the intestinal villus by

staining whole-mount mouse intestines for active (phosphorylated) Myosin-II, the primary force-generating motor protein. We observed a pronounced accumulation of Myosin-II at the basal surface of villus cells, which increased from the base to the tip (**Fig. 1I-L & fig. S2A-D**). This Myosin-II accumulation suggested the generation of tensile forces, prompting us to question whether compression forces prevail at the villus tip.

To test if the intestinal epithelium at the villus tip was under tension or compression in vivo, we dissected small intestines from wild-type mice and immediately afterwards applied line-shaped laser ablations at different regions of the villus: If the tissue were under tension, one would expect an outward retraction orthogonal to the cut line, whereas a compressed tissue would shrink or remain static (**Fig. 1M**). In one set of experiments, we ablated the basal surface of a lateral group of 6–10 adjacent cells using a line cut spanning ~60 μm (**fig. S2E-F**) – sizeable enough to integrate the response of multiple cells, yet within the geometric constraints imposed by the villus curvature (*32*). These cuts were performed both at the villus shaft and at the villus tip region. Upon ablation at the basal surface, we observed a rapid outward tissue recoil orthogonal to the ablation line in both regions (**Fig. 1N-P, fig. S2F & Movie S2**) with a similar maximum recoil and initial recoil velocity of approximately 1.4 μm/s (**Fig. 1Q, R**). In another setup, we ablated entire single cells along their apical–basal axis at the villus tip, rather than cutting only their basal surface. Here too, neighboring cells consistently retracted away from the ablated cell (**fig. S2G-J)**. Thus, the mouse villus tip, the main region of cell extrusion, is under tension rather than compression.

A highly dynamic actomyosin network underlies basal tissue tension.

Given the above findings and the known cytoskeletal remodeling required for cell extrusion, we hypothesized that local tensile tissue forces could play a role in its regulation. We generated

intestinal organoid reporter lines for Myosin-II by integrating a fluorescent tag (mNeonGreen) in the endogenous locus of different subunits of the Myosin-II multiprotein complex (**Fig. 2A, B & fig. S3A-D**). The reporter targeting myosin regulatory light chain (Myl12a) co-localized strongly with antibodies for active (phosphorylated) Myosin-II (**fig. S3E, F**). It was also enriched at sites of actomyosin contraction, for example at the cytokinetic furrow during cell division (**fig. S3G**). During cell extrusion, Myosin-II rapidly increased at the cell base and redistributed in a zipper-like pattern along the lateral surface towards the apex, before the cell was expelled apically into the organoid lumen (**Fig. 2C, fig. S3H & Movie S3**). This suggests that Myosin-II-mediated contraction exerts the force necessary to extrude a cell into the lumen.

The Myosin-II intensity profile along the organoid's crypt-villus axis showed a strong apical signal in the crypt region, diminishing towards the villus domain (*33*, *34*) (**fig. S3I, J & Movie S4**). Conversely, basal Myosin-II exhibited its highest intensity in the villus region, both in organoids and in tissue (**Fig. 1L & fig. S3I, J**). Stimulated emission depletion (STED) super-resolution microscopy identified two distinct Myosin-II localization patterns: a junctional pool, which lined the cell boundaries and predominated the apical surface; and a medial pool where Myosin-II coalesced in the cell center and extended radially to cell-cell junctions, predominantly found at the basal cell surface in the villus domain (**Fig. 2D, E**). The overlap of medial and junctional Myosin-II at the basal surface creates an interconnected actomyosin network, similar to those facilitating coordinated cell movements in other epithelial tissues (*35*, *36*). We confirmed that this organization was also prevalent in vivo throughout the intestinal villi, both in the shaft region and at the villus tip (**Fig. 2F & fig. S3K**). The prominent basal enrichment of both medial and junctional Myosin-II suggests a network capable of generating tissue tension through coordinated contractions (*37*, *38*).

To reconstruct the force-transmission between cells in an in vivo-like fashion, we grew Myosin-II reporter organoids on 3D hydrogel substrates that closely mimic the tissue architecture of the intestine (**Fig. 3A & fig. S3L**) (*8*). Live-cell imaging of the synthetic villus tip showed dynamic basal myosin-II remodeling, revealing a pulsatile reorganization of the actomyosin network on the basal surface of the intestinal epithelium (**Fig. 3B-F, fig. S4A-E & Movie S5**). With our earlier data, this suggested that while the tissue is permanently under tension, individual cells' contractility dynamically changes. This is reflected in transient Myosin-II accumulation that was accompanied by a concomitant decrease of basal cell area presumably owing to the Myosin-II-mediated pulling forces (**Fig. 3C-F, fig. S4A-E**). Conversely, basal expansion was accompanied by decreasing Myosin-II levels, and Myosin-II minima coincided with an increase of basal area. (**Fig. 3C-F, fig. S4A-E**). Pulsatile actomyosin networks have been described in other epithelia to coordinate cellular rearrangements such as the inward folding of a tissue (*37*, *38*) or delamination of individual cells (*39*). These dynamics allow cells to continuously interact with their neighbors, probe the environment, and enable tissue-level coordination (*38*, *40*). Such tissue-level coordination was evident in the inverse relationship between the cell areas of neighboring cells: when a central cell constricted, its neighbors expanded (**fig. S4F, H**). Thus, cells in the villus region dynamically regulate Myosin-II, driving pulsatile basal area changes. Through mechanical coupling via cell junctions, Myosin-II-generated forces appear to propagate to adjacent cells, orchestrating a tissue-wide tug-of-war.

Cell extrusion is regulated by a cell's ability to exert tissue tension

To determine whether tissue tension generated by basal actomyosin contractions has a role in regulating cell extrusion, we established an optogenetic method to control Myosin-II-mediated

contractility, and thereby tissue tension, in intestinal organoids. We integrated a doxycycline-inducible optogenetic system called opto-Arhgef11 (*41*) into intestinal organoids. Opto-Arhgef11 is based on the light-dependent heterodimerization of the photosensor CRY2, fused to the small RhoGTPase Arhgef11, and its interaction partner CIBN, which is anchored at the plasma membrane (**Fig. 4A**). Arhgef11-CRY2 remained cytoplasmic and inactive in the dark, but rapidly translocated to the plasma membrane upon blue light excitation (**Fig. 4B**). On the membrane it initiated the endogenous Rho signaling cascade, which triggers Myosin-II-induced cell contractility and increases tissue tension. Indeed, local photoactivation caused a focused contraction of the organoid, which relaxed again owing to the dissociation of CRY2-CIBN in the absence of blue light (**Fig. 4C & Movie S6**). Staining uniformly photoactivated opto-Arhgef11 organoids for phosphorylated Myosin-II revealed a ~1.7-fold overall increase in active Myosin-II levels, with minimal impact on its subcellular distribution (**fig. S5A-C**).

To test the impact of Myosin-II activity on cell extrusion systematically, we grew opto-Arhgef11 organoid cells on synthetic 3D hydrogel substrates and measured the rate of extrusion at the villus tip (**Fig. 4D & fig. S4C**). Continuous global photoactivation led to increased tissue tension compared to non-activated villi (**fig. S5D-F**) and resulted in a 5-fold increase in the average extrusion rate (**Fig. 4E & fig. S5G-J**). The increase of extrusion rates upon photoactivation was dependent on the addition of doxycycline, confirming that it was not caused by phototoxicity (**fig. S5G**). The extrusion rate increased readily upon photoactivation, directly following the overall increase of tissue tension. This suggested a link between the tension exerted by cells on their neighbors and extrusion. To test the effect of contractility differences between neighboring cells, we photoactivated one half of the optogenetic villus tip, creating an artificial boundary between Myosin-induced and non-induced cells (**Fig. 4F, G)**. Cell extrusion was increased locally along the

boundary of photoactivation (**Fig. 4H-K)**. Cells most frequently extruded in the non-activated area facing the boundary with the photoactivated area, while cells adjacent to the boundary in the photoactivated region extruded less frequently in comparison (**Fig. 4J)**. Extrusion events were evenly distributed along the photoactivation boundary, indicating that the effect was specific to the illumination pattern (**Fig. 4K)**. Thus, individual cells with lower contractile capabilities compared to the surrounding tissue appear to be more prone to extrusion.

To test this hypothesis, we generated mosaic organoids containing varying ratios of wild-type (WT) cells (tagged with H2B-iRFP or H2B-mCherry nuclear markers) and opto-Arhgef11 organoid cells (**Fig. 5A**). Upon photoactivation, WT cells were significantly overrepresented among extruded cells, particularly in mosaics where WT cells were present as a minority. To quantify this effect, we compared the fraction of WT cells in the extruded population to their overall presence in the organoid, referred to as extrusion enrichment. In organoids where WT cells represented the majority, their extrusion occurred approximately at a rate proportional to their abundance (**Fig. 5B**). However, as the proportion of opto-Arhgef11 cells increased, WT cells were extruded at a disproportionately higher rate resulting in a 4-fold extrusion enrichment (**Fig. 5B**). This imbalance was not observed in control organoids that were not induced with doxycycline or not exposed to blue light – in these cases WT cell extrusion rates remained proportional to their overall presence in the organoid (**Fig. 5C**). When examining mosaic organoids with a WT cell majority (> 50%), the probability of WT cell extrusion increased with their local proximity to opto-Arhgef11 cells (**Fig. 5D**). Thus, when optogenetic cells form the majority, the increased tissue-level tension enhances mechanical competition and drives the preferential extrusion of less contractile WT cells. This effect is further reinforced at the local level, because WT cells are more likely to extrude when close to highly contractile optogenetic cells.

To further substantiate these findings, we created a Myh9 heterozygous knockout (*Myh9*$^{+/-}$) organoid line, which has genetically impaired Myosin heavy chain function (*33*, *42–45*) (**Fig. 5E & fig. S5K, L**). When *Myh9*$^{+/-}$ were combined with wild-type cells in 3D mosaic organoids, WT cells were consistently underrepresented among extruded cells, while *Myh9*$^{+/-}$ cells were overrepresented (**Fig. 5F-I**). The observation that *Myh9*$^{+/-}$ extrusion enrichment progressively increased with higher WT cell content argued that higher organoid-level tension promotes the preferential removal of less contractile cells (**Fig. 5I**). Indeed, when two Myh9$^{+/–}$ populations labeled with different nuclear markers (H2B-mCherry and H2B-GFP) were combined – hence eliminating contractility differences – no extrusion bias was observed (**Fig. 5J, K**). Thus, cells appear to assess their neighbors' ability to generate tension continuously, resembling a tug-of-war competition for extrusion of weaker cells.

Disruption of the basal cortex integrity causes cell extrusion.

To test this "tug-of-war" hypothesis at the cellular level, we used infrared (IR) laser microsurgery (*33*, *46*) to destabilize the basal cell cortex of individual cells in the villus region (**Fig. 6A, B**). Disrupting the basal cytoskeleton consistently led to the extrusion of the targeted cell within one hour (**Fig. 6C-G, Movie S7**), whereas applying the same laser stimulus directly to the nucleus had no such effect (**Fig. 6E-G & Movie S8**). In line with our finding that villus cells are under tension, basally targeted cells expanded within 15 seconds of ablation, indicating a rapid release of basal tension, while expansion was absent when ablation was instead targeted to the nucleus (**Fig. 6I**). The magnitude of the basal area expansion correlated with the probability of subsequent cell extrusion (**Fig. 6J**), but not with the extrusion time (**Fig. 6K**). The reliable induction of cell

extrusion following basal expansion further supported the notion that a critical loss of tension-generating capacity owing to cytoskeleton disruption is necessary to trigger extrusion.

Directly after basal microsurgery, basal Myosin-II levels accumulated at the lateral cell boundaries accompanied by a contraction of the basal surface that brought together the membranes of neighboring cells (**Fig. 6L, M**). When Myosin-II activity was inhibited pharmacologically with blebbistatin, the probability that cells extruded at all within one hour decreased from 83% in control organoids to 51% in blebbistatin-treated organoids (**Fig. 6N**), while the duration of the extrusion process after basal microsurgery increased ~2-fold (**Fig. 6O, P**). Thus, Myosin-II activity is required for executing cell extrusion and for the timely removal of mechanically weakened cells.

Next, we examined the cellular response when applying the laser stimulus to tension-bearing bi- or tri-cellular basolateral junctions (**Fig. 6Q**). This procedure reliably induced the simultaneous extrusion of a duplet or triplet of cells, respectively, showing that the mechanical destabilization of multicellular junctions led to the simultaneous extrusion of the affected cells (**Fig. 6R, fig. S6A-F & Movie S9**). Again, when we inhibited Myosin-II activity with blebbistatin and destabilized the bases through microsurgery, only 51% of the cells extruded within 1 hour, compared to 83% without inhibition (**fig. S6G-I**). The stimulated multi-cell extrusion was driven by the contraction of a common actomyosin accumulation that enclosed all extruding cells (**fig. S6J**). E-cadherin junctions in neighboring cells were maintained (**fig. S6K**) and the overall extrusion rate at the organoid level did not significantly increase (**fig. S7A-C**), indicating that the epithelial barrier and tissue integrity was maintained. Thus, the epithelium appears to eliminate groups of neighboring cells when they become mechanically compromised and lose the ability to maintain junctional tension.

This prompted us to investigate whether extrusion is driven by cell-autonomous contraction or the coordinated contraction of adjacent cells. We generated mosaic organoids composed of Myosin-II reporter cells and cells expressing only a nuclear marker and analyzed reporter cells surrounded by non-labelled neighbors (**Fig. 6S**), as well as non-labelled cells surrounded by reporter neighbors (**Fig. 6T**). Myosin-II levels increased drastically in spontaneously (i.e. non-ablated) extruding cells, but also in the cell neighbors (**Fig. 6U & Movie S10**). Thus, the extruding cell appears to trigger an endogenous response to drive its own extrusion through Myosin-II upregulation supported by the coordinated Myosin-II upregulation in adjacent cells. Together these processes reflect a coordinated tissue behavior to achieve proper contraction, extrusion, and maintenance of epithelial integrity. Thus, intestinal cell extrusion is a coordinated tissue behavior.

Epcam loss distorts tissue tension and epithelial homeostasis in tufting enteropathy.

Dysregulation of contractility-based tissue coordination can profoundly impact tissue homeostasis. For example, congenital tufting enteropathy (CTE) is a rare genetic disorder characterized by severe, intractable diarrhea in infants, often leading to intestinal failure. It is caused by mutations in *Epcam* (*47*, *48*), which encodes a negative regulator of Myosin-II: its loss leads to Myosin-II hyperactivation (*49*, *50*). The disease phenotype includes impaired intestinal barrier function, epithelial defects, and disrupted tissue organization, such as villous atrophy, crypt hyperplasia, and focal epithelial tufts (**Fig. 7A**) (*51*). These tufts are distinct histological features characterized by the disorganization and crowding of surface enterocytes into tuft-like structures.

To investigate the potential role of our proposed extrusion regulation mechanism in CTE, we introduced Epcam loss-of-function mutations in intestinal organoids using CRISPR/Cas9,

generating three independent *Epcam*$^{-/-}$ lines (**Fig. 7B, C & fig. S8A**). Mutant organoids displayed distorted morphology: the well-structured morphology of wild-type organoids, characterized by distinct budding protrusions and a cystic center, was largely lost in *Epcam*$^{-/-}$ organoids (**Fig. 7C, D & fig. S8B, C**). Time-lapse imaging of *Epcam*$^{-/-}$ organoids growing from small cystic organoids over several days revealed repeated cycles of inflation and deflation (**Movie S11**). Compared to wild-type organoids, *Epcam*$^{-/-}$ organoids exhibited delayed budding, initiating bud formation after three rather than two days. Additionally, they grew into noticeably larger structures than WT organoids (**fig. S8C**). Using qPCR and immunofluorescence, we confirmed that *Epcam*$^{-/-}$ organoids differentiated into all major intestinal lineages but exhibited some marked differences (**fig. S8D, E**): Consistent with CTE's crypt hyperplasia, *Epcam*$^{-/-}$ organoids showed increased expression of markers for stem cells and immature enterocytes, and a reduction in markers of mature cell types in comparison to WT organoids (**fig. S8D, E**). These findings align with reports of delayed differentiation and persistent differentiation defects in CTE (*52*, *53*).

The reduced presence of mature cell types could be attributed to increased cellular turnover. To investigate this, we measured cell extrusion rates using a transwell assay and flow cytometry. *Epcam*$^{-/-}$ organoids exhibited a ~1.5-fold increase in extrusion rate compared to WT (**Fig. 7F**) and immunostaining for phospho-Myosin-II confirmed myosin hyperactivation (**Fig. 7G & fig. S8F, G**). Our findings that excessive contractility and elevated tissue-level tension accelerated cell extrusion (**Fig. 4D, E**) suggested that Epcam loss may contribute to epithelial dysregulation by increasing mechanical tension, which could promote premature cell removal and thereby manifest the disease phenotype.

To examine the effects of contractility differences in this disease-relevant context, we generated mosaic organoids containing WT and *Epcam*$^{-/-}$ cells and analyzed cell extrusion. Live imaging and quantification of extrusion enrichment revealed that hypercontractile *Epcam*$^{-/-}$ cells extruded less frequently, while WT cells were overrepresented among extruded cells. This effect became stronger with increasing abundance of *Epcam*$^{-/-}$ cells (**Fig. 7H, I**). This mirrored our earlier finding with WT and opto-Arhgef11 cells, where the less contractile minority population was preferentially extruded (**Fig. 5B**). Combining two WT lines with different nuclear markers did not show such biased extrusion (**Fig. 7J**), confirming that contractility differences rather than genetic labels drive extrusion. To determine whether Myosin-II hyperactivation directly drives competitive extrusion, we inhibited Rho signaling pharmacologically using Y16 (Rho-GEF inhibitor) and Y-27632 (ROCK inhibitor) in mosaic *Epcam*$^{-/-}$/WT organoids with a majority *Epcam*$^{-/-}$ cells. Both inhibitors significantly reduced WT extrusion enrichment, demonstrating that suppressing Myosin-II activity alleviates the extrusion bias against WT cells (**Fig. 7K**). Thus, tension heterogeneity within the epithelium drives cell extrusion and differences in Myosin-II–mediated contractility create mechanical competition that determines which cells are extruded. This process, when dysregulated, may contribute to epithelial pathologies such as congenital tufting enteropathy.

Discussion

The self-renewal of the intestinal epithelium is commonly described using the analogy of a conveyor belt: cells are continuously produced in intestinal crypts, move into the villus domain as they differentiate, and finally extrude into the lumen from the villus tip. In line with this model, it has been suggested that cells extrude in response to tissue crowding as they ultimately accumulate at the villus tip, where owing to the limited space, the tissue is compressed (*20*, *21*). Our findings

challenge this model: instead of tissue compression, we find that the basal surface of intestinal villi, including the tip region, is under tension. This tension is mediated by Myosin-II pulsations in the basal cytoskeleton, and cell extrusion rates are directly coupled to this tissue-level tension. Laser ablation of the cell base, causing local weakening, or genetic impairment of contractility both induce extrusion, suggesting that cells unable to sustain tension are eliminated. In contrast, (opto-)genetic activation of Myosin-II increases tissue-wide tension and amplifies the mechanical competition between cells, promoting the preferential extrusion of weaker cells. These complementary approaches reveal a shared principle: A cell extrudes when it can no longer sustain or reciprocate the tension exerted by neighboring cells – whether due to a local impairment of contractility or increased tension exerted by its neighbors.

In the intestine, an interconnected basal actomyosin network facilitates the transmission of physical forces throughout the villus epithelium, coordinating tissue-level behaviors such as cell extrusion, as shown here, but potentially also cell migration (*3*) and proliferation (*54*, *55*). Indeed, a cell's extrusion triggers cell contractility in its neighbors and impacts tissue-level tension. We propose a revision of the roles of cell extrusion and proliferation in tissue homeostasis. Cells at the villus tip are not pushed into crowding and compression but instead pull on their neighbors driving a mechanical competition, leading to the preferential extrusion of less contractile ("weak") cells. Hence, the intestinal epithelium acts as a self-renewing network of cells that autonomously replaces its weakest links. Indeed, cell extrusion thus not only serves to maintain cell number homeostasis, but also serves to maintain "mechanical homeostasis" – the need to maintain and restore the optimal mechanical tissue state. Mechanochemical signaling dynamics driven by Myosin-II-mediated tissue tension thus complements biochemical signaling gradients in the organization and maintenance of intestinal homeostasis. This tissue-level tension caused by the

extrusion of weak cells could, in turn, promote cell proliferation and thus proliferation may respond to extrusion to maintain cell number homeostasis, rather than driving extrusion. This would invert the conventional view of cause and effect in intestinal homeostasis. Indeed, increased tissue tension in intestinal organoids (*54*, *55*), MDCK monolayers (*56*), mouse colon (*57*) or the pig intestine (*58*) can stimulate cell proliferation.

While the role of tensile basal actomyosin has been recognized in morphogenesis (*59–61*), we show its importance for intestinal barrier maintenance during tissue homeostasis. This has implications for pathologies in which the epithelial barrier function is impaired, beyond the tufting enteropathy studied here. For example, mutations in cytoskeletal components such as Myosin IIA heavy chain (*62*), RAC1 (*63*), Myosin IXB (*64*), Keratin 8 (*65*) and cytoskeletal crosslinking protein ACF7 (*66*) are associated with increased epithelial permeability and are implicated in diseases characterized by excessive cell extrusion such as inflammatory bowel disease (Crohn's disease and Ulcerative Colitis). On the other hand, cancerous epithelial cells evade homeostatic cell extrusion and initiate primary tumors by distorting extrusion mechanisms and extruding through the basal rather than the apical surface (*67*, *68*). Mutation of RAS oncogenes – prime drivers of small intestinal adenocarcinomas (*69*) – interfere with Myosin-II activity and alter tissue mechanics (see ref. (*70*) for review). Based on our findings, we propose tissue tension as a potential therapeutic target that could be influenced through pharmacological modulation (*71*) to alleviate excessive shedding in the context of inflammatory bowel disease (IBD) or to accelerate the extrusion of cells that threaten intestinal integrity, e.g. during pathogen infections (*72–74*).

Materials and Methods

Organoid culture

Organoids were grown in basement membrane extract (BME; Biotechne R&D Systems; cat. #3533-010-02) and ENR growth medium. ENR growth medium was prepared with murine recombinant Noggin (100 ng/mL; ThermoFisher, cat. #250-38-100UG) and human recombinant R-spondin 1 (500 ng/mL; ThermoFisher, cat. #120-38-5UG), 1 mM n-acetylcysteine (Merck, cat. #A9165-5G), 50 ng/mL epidermal growth factor (EGF; ThermoFisher cat. #315-09-500UG), N2 and B27 supplement (1×; ThermoFisher, cat. #17502048 and #17504044, respectively), Glutamax (2 mM; ThermoFisher cat. #35050061), HEPES (10 mM; ThermoFisher, cat. #15630080), 100 U/mL Penicillin, 100 µg/mL Streptomycin (Penicillin-Streptomycin, Gibco Thermo Fisher Scientific, cat. #11548876) in Advanced DMEM/F12 (ThermoFisher, cat. #12634010). Passaging was done once and the medium change two times per week on non-consecutive days. During passaging, BME was dissolved in cold base medium (2 mM Glutamax, 10 mM HEPES in Advanced DMEM/F12) and organoids were mechanically disrupted, before embedding in new BME and plating onto a culturing plate. BME was left to solidify for 20-30 minutes before new growth medium was added. For expansion and outgrowth of single cells, organoids were cultured in Wnt-conditioned medium (ENR, 10 mM Nicotinamide (Sigma-Aldrich, cat. #98-92-0), home-made Wnt3A conditioned medium 50% (v/v) (*75*)). Organoids expressing the optogenetic module were kept in the dark in an aluminum vessel. To inspect optogenetic organoids, culture plates and dishes were placed in containers wrapped in Deep Amber lighting filter foil (Cabledelight) to filter blue light.

Cloning

Gibson Assembly (NEBuilder HiFi DNA Assembly, NEB, cat. # E2621) was used for the cloning of all constructs. Transgenic constructs were cloned into p2T vectors that flank the inserts with 3' and 5' tol2 sequences. These transposable elements mediate the mT2TP transposase-dependent random integration of the expression constructs into the cell genome. For p2T-CIBN-GFP-Puro^R, a new p2T vector was assembled by combining fragments containing an empty p2T backbone, the CAG promoter, CIBN-GFP (from ref. (*76*) and IRES-Puro^R. To express Arhgef11-CRY2 under Dox-inducible promoter, in a p2T backbone, the Tet-ON 3G transcription factor driven by a CMV promoter (from ref. (*77*)) was combined with a P2T-T2T tandem and a Hygromycin^R. In opposite direction, a TRE3GS promoter (from ref. (*77*)) was cloned to drive the PHR-CRY2 domain fused to Arhgef11 (from Addgene plasmid #89481) and followed by a SV40 polyA tail. A second construct containing Argef11-mCherry-CRY2 was generated based on the p2T-TetON-Hygro-Arhgef11-CRY2 construct. For p2T-H2B-iRFP-IRES-Puro^R and p2T-H2B-mCh-IRES-Blast^R nuclear markers, the p2T-CIBN-GFP-Blast^R construct was cut with XhoI and BsrGI (both New England Biolabs, cat. #R0146S, #R3575S) and fragments containing H2B, iRFP670 or mCherry and IRES-Blasticidin^R were combined. p2T-CMV-H2B-eGFP-SV40-Hygro^R was assembled to contain the p2T backbone, a CMV promoter driving H2B-mEGFP and a SV40 promoter driving a Hygromycin^R. Two new CRISPR-HOT donor plasmids were generated. Based on pCRISPaint-mNeon (Addgene plasmid #174092), new donors containing pCRISPR-HOT-mNeon-P2A-T2A-mCherry-CAAX (to generate mNeonGreen fusion protein that co-translates a red-fluorescent plasma membrane marker), pCRISPR-HOT-mNeon-Stop-PGK-mCherry-CAAX (to generate mNeonGreen fusion protein and expresses a red-fluorescent plasma membrane marker independently under the PGK promoter) were generated using Gibson assembly.

CRISPR-mediated reporter and knockout generation

Knock-in reporter organoids were generated using CRISPaint technology (*78*) and the CRISPR-HOT method (*79*). A gene-specific sgRNA-containing plasmid (**Table S1**) was co-transfected (*80*) with a donor plasmid containing the fluorescent tag and the frame-selector plasmid containing an sgRNA to linearize the donor plasmid and the Cas9 into mouse intestinal organoids (each 5 µg sgRNA plasmid) using a NEPA electroporation system (NEPAGENE). Myosin knock-in reporter organoids were generated using both pCRISPR-HOT_mNeon-P2A-T2A-mCherry-CAAX and pCRISPR-HOT_mNeon-Stop-PGK-mCherry-CAAX donor vectors. The Comparison of the target-specific co-expression and independent expression of the mCherry plasma membrane marker allowed an estimation of signal strength and localization across gene targets. Myl12a-mNeonGreen-P2A-T2A-mCherry-CAAX was selected to characterize myosin activity and dynamics in organoid tissue. In addition, pCRISPR-HOT_tdTomato (Addgene plasmid #138567) was used to generate a Myl12a-tdTomato line and pCRISPaint-mNeon in combination with a Cdh1-specific sgRNA was used to generate a live reporter for E-cadherin. Three days before and two weeks after electroporation organoids were split and cultured in Wnt-conditioned medium. Expression of fluorescent reporters in individual organoids was monitored daily. To generate stable organoid lines, fluorescent organoids were picked, dissociated to single cells using TrypLE Express Enzyme (Thermo Fisher Scientific, cat. #12605010) and expanded for two weeks in Wnt-conditioned medium. Stable lines were cultured in ENR medium.

For gene-specific knockout generation, a sgRNA vector conferring a transient Hygromycin and a Cas9 vector conferring a transient Puromycin resistance were co-transfected. After electroporation organoids were cultured in Wnt-conditioned medium. One day after electroporation the organoids were exposed to Puromycin (2 µg/ml; InvivoGen, cat. #ant-pr) and Hygromycin B Gold (100

µg/ml; InvivoGen, cat. #ant-hg) for 24 h. Two weeks after electroporation outgrown organoid clones were picked, dissociated to single cells, DNA was extracted using Quick-DNA Microprep Kit (Zymo Research Corporation, cat. #D3021) and genotyped using gene-specific primer pairs (sanger sequencing performed by Macrogen Europe BV). Clonal organoid lines were cultured in ENR medium.

Generation of transgenic organoids

Organoid lines expressing H2B nuclear marker (*30*, *81*), Dox-inducible optogenetic modules and the optogenetic anchor CIBN-GFP were generated by co-electroporation of 5 µg of the respective expression construct and 5 µg of a vector containing the mT2TP transposase driven by the CAG promoter for the transient expression of mT2TP mediating the tol2-dependent genome integration of expression constructs. One week after electroporation organoids were exposed to the expression construct-conferred resistance. The culture was propagated and maintained in ENR medium containing the expression construct-conferred resistance.

Sample preparation of synthetic hydrogels with crypt-villus topology

ECM-based hydrogel substrates were generated as described previously (*8*). Before organoid seeding, the substrates attached to 35 mm culture dishes were sterilized using UV illumination and repeated washes using PBS solution containing Primocin (1:500; InvivoGen, cat. #ant-pm) and incubated in Wnt-conditioned medium overnight. Cells were incubated in Wnt-conditioned medium three days before seeding. For cell seeding, BME was enzymatically digested using Dispase (Stemcell Technologies cat. #07913) and washed away using cold base medium. Cells were dissociated to single cells using Accutase Cell Detachment Solution (Innovative Cell Technologies, cat. #AT104-500), pelleted by centrifugation at 250xg for 5 min and resuspended in

15 µl of Wnt-conditioned medium. Medium was aspirated from substrates and the cell suspension was seeded evenly onto the surface. Cells were allowed to attach for 5 min at 37°C before more Wnt-conditioned medium containing 10 µM Y-27632 (Abmole, cat. #M1817) was added to fill the culture dish. The cells were kept in Wnt-conditioned medium for four days, in Wnt-conditioned medium diluted 1:2 in ENR for three days and eventually kept in ENR medium. Organoids expressing the optogenetic modules were kept in medium containing Puromycin (1 µg/ml) and Hygromycin B Gold (100 µg/ml) and incubated in a dark aluminum chamber and inspected through blue-light filtering foil.

Generation of mosaic organoids

Two organoid lines were dissociated to single cells as described for seeding on hydrogel substrates, resuspended in Wnt-conditioned medium and combined at desired ratios. The cell suspension containing 300k cells in 20 µl medium was mixed well by repeated pipetting and 20 µl were seeded per well onto a 48-well-plate. The plate was spun at 200xg for 5 min and incubated for 30 min at 37°C before Wnt-conditioned medium (with 10 µM Y-27632) was added. After 24 h the cell layer was mechanically detached by scaping of the cell layer using a pipette tip and repeated flushes with base medium. Without extra mechanical sheering, the cells were collected by centrifugation and seeded directly into microscope sample carriers. Organoids were cultured in ENR medium. Mosaic organoids were imaged for 12-20 h using a Leica Stellaris confocal microscope or Viventis Light sheet microscope.

Extrusion measurement of *Epcam*$^{-/-}$ and wild-type cells

Transwell inserts with 0.1 µm pore size (Corning, cat. #CLS3396) were coated with 5% BME for 30 minutes. Organoid cells were dissociated into single cells as described above, resuspended in

Wnt-conditioned medium supplemented with 10 µM Y-27632, and seeded onto the transwell surface at a density of 200,000 cells per insert. The cells were cultured for four days in Wnt-conditioned medium to achieve full confluency, followed by two days in transition medium (1:1 mix of ENR and Wnt-conditioned medium). To promote differentiation, monolayers were then maintained for 10 days in ENR medium. Only transwells with complete and confluent monolayer coverage were included in downstream analysis. Flow cytometry was used to count extruded cells in the medium covering the monolayer. To this end, the medium covering the monolayer was refreshed and collected after 1, 2, and 3 hours. The cells were stained with DAPI (1 µg/ml) and the number of extruded cells was measured by FACS using a CytoFLEX (Beckman Coulter). To normalize extrusion rates to the number of cells in the monolayer, the transwell membranes were fixed in 4% paraformaldehyde for 30 minutes at room temperature, washed with PBS, and stained with DAPI (1 µg/ml). Whole-membrane tile scans were acquired using a Leica Thunder widefield microscope with a 5× air objective. Cell nuclei were segmented using StarDist in Fiji, and total cell numbers were quantified. The extrusion rate was calculated as the number of extruded cells (by FACS) divided by the total number of monolayer cells (by image segmentation), normalized to the time of sample collection.

Long-term live-cell imaging and image analysis

For long-term live imaging of nuclear reporter organoids, organoids were seeded onto an imaging chamber (CellVis 4 Chambered Coverglass System cat. #C4-1.5H-N) and imaged on a A1R MP (Nikon) scanning confocal microscope outfitted with a 1.30 NA 40× magnification oil immersion objective, incubation chamber set to (37 ºC, 5% CO_2) (*30*). Images were taken every 12 minutes, and at each timepoint, 31 Z-slices were imaged with 2 µm intervals.

For live imaging of organoids grown on synthetic crypt-villus substrates, the chips were placed into a µ-Dish 35 mm glass bottom dish (Ibidi, cat. #81218-200) onto a circular holder made of PDMS material with a width of ~2 mm. The samples were imaged using a Leica SP8 confocal microscope using a HC PL APO CS2 20x/0.75 air objective at 37 ºC and 5% CO_2. Z-Stacks of 40 µm were collected with 1 µm Z-interval and with a time interval of 6 min.

Epcam$^{-/-}$ and wild-type organoids were seeded on a 96-well glass bottom plate and imaged over a period of 1 week using a Leica Thunder widefield microscope using a 5X air objective and brightfield illumination.

Cell tracking

Semi-automated tracking of single cells and their extrusion from organoids was done by tracking the cell nuclei using the OrganoidTracker (*29*) software. Tracks and lineage trees were analyzed in Python. Cells were censored when they moved out of view or were still alive when the image acquisition was stopped. We measured the cell density around a cell as the inverse of the average distance to its six closest neighbors (in millimeters), using the *cell_density_calculator* in OrganoidTracker (*29*).

Optogenetic experiments

Photoactivation of opto-Arhgef11 organoids was done using a Leica SP8 confocal microscope using a HC PL APO CS2 40x/1.10 water objective. 3D organoids expressing the system were imaged first using only 640 nm excitation to collect transmitted light and the H2B-iRFP nuclear marker signal (pre-activation). For regional photoactivation a region of interest (ROI) was designed, which was set to be illuminated with low intensity of 488 nm light (0.5-1%). A time course with a time interval of 1 seconds was started with simultaneous illumination of the entire

organoid with 640 nm excitation (to collect transmitted light and the H2B-iRFP nuclear marker signal) and 488 nm-photoactivation specific to the ROI. In this region, the GFP signal of the labelled optogenetic anchor was recorded. To stop photoactivation, the laser power of the 488 nm laser was set to zero. To record the translocation of Arhgef11-CRY2-mCherry to the plasma membrane, a Zeiss LSM780 was used with a C-Apochromat 40x/1.20 W Korr M27 water objective (Zeiss). First, the mCherry signal was collected using 564 nm excitation, then a region was illuminated within a ROI using 488 nm illumination and the mCherry signal was collected again after 5 seconds. For the photoactivation of optogenetic organoids grown on synthetic hydrogels, a Leica SP8 confocal microscope using a HCX IRAPO L 25x/0.95 water objective was used. A water pump was attached to the water immersion objective that compensated for water evaporation during the experiments. As a control, we first imaged optogenetic organoids on hydrogel substrates that were not induced by doxycyclin before for 2.5 h at a time interval of 4 min with both 640 nm light to record the H2B-iRFP nuclear signal and 488 nm blue light. The positions of the imaged villi were saved. Afterwards the organoids were incubated for 12 h to let them recover, induced with 1 µg/mL doxycyclin (Thermo Fisher Scientific, cat. #10592-13-9) for 24 hours and the same villi were imaged for 2.5 h only with 640 nm light without 488 nm. Again, the organoids were incubated for 12 h and the villi were imaged for 2.5 h with both 640 nm and photoactivated using 488 nm light. Extrusions were counted and the extrusion rates were calculated for each villus. In another setup, the samples were first imaged for 2.5 h exclusively with 640 nm light (non-activation), followed by 2.5 h with simultaneous photoactivation using 488 nm light in time intervals of 4 min. Similar to the localized photoactivation in 3D organoid cultures, for the patterned photoactivation of only one half of the villus tip, the villus tip was centered and imaged in the full field of view using 640 nm light, while only the left half of the tip was illuminated with 488 nm for 2.5 h. Mosaic organoids were imaged using a Leica Stellaris Confocal microscope using a 20X air objective

(20x/0.75 Air, Leica) or using a Viventis Light sheet microscope, as described below, and photoactivated every 5 min. For all optogenetic experiments: To be able to position the optogenetic samples at confocal microscopes a deep Amber lighting filter foil (Cabledelight) was placed on top of the condenser to block blue light from brightfield illumination.

Light sheet imaging

Live imaging of Myo-mNG reporter organoids and mosaic organoids was performed using a LS1 Live light sheet microscope (Viventis Microscopy) using a Nikon 25X NA 1.1 water immersion objective at a magnification of 18x. Organoids were mounted on a single-chamber sample holder one day before the start of imaging. Organoids were imaged at 37°C and 5% CO_2. A position-specific alignment of the light sheets with a thickness of 2.2 µm was done. Organoids were imaged every 8 minutes using appropriate laser lines depending on the fluorophores expressed. Myo-mNG reporter organoids were imaged with 488 nm and 561 nm illumination. Mosaic organoids expressing combinations of H2B-mCherry, H2B-iRFP, H2B-GFP, or CIBN-GFP were imaged using 561 nm, 638 nm, and 488 nm illumination, respectively. Organoids co-expressing Myo-mNG with H2B-iRFP, or Myo-tdTomato with H2B-GFP and H2B-iRFP, were imaged using 488 nm and 638 nm, or 488 nm, 561 nm, and 638 nm illumination, respectively. Post-acquisition analysis was performed using Fiji.

Image analysis of short-term movies

Image processing and analysis was done using Fiji (*82*)/ImageJ2 (*83*). To measure the basal expansion after laser-ablation of the basal cytoskeleton, organoids expressing H2B-mCherry and E-cadherin-mNeonGreen were plated onto an imaging plate (day 0) and ablated at the base on day 2. The time-lapse video of the stimulation was taken from 5 seconds before stimulation until

15 seconds after stimulation, and the basal area of the ablated cells was measured on the average E-cadherin-mNeonGreen signal before (-5 s < t < 0 s) and after (10 s < t < 15 s) ablation. 3D renderings were generated by exporting nuclei positions from OrganoidTracker and rendering in ParaView (v. 5.11.0).

The basal surface of reporter organoids grown on synthetic crypt-villus substrates was extracted using the Fiji plugin LocalZProjector (*84*). Basal cell membranes were segmented and tracked manually using Napari (napari.org) and analyzed in Matlab (2021b, MathWorks). Myosin levels were quantified using Matlab by creating binary masks for individual cells and timepoints to calculate the cell area and mean fluorescent signal. Graphs were visualized using the *plot* function and smoothened with a factor of 3. To identify myosin or basal area peaks (primary parameter), a trend curve was calculated and subtracted from the raw signal before maxima were identified using the *findpeaks* function. To calculate the trend, a polynomial function of 4^{th} degree was fitted to single cell myosin/basal area curves (signal over time) using the *fit* function. The corresponding secondary parameter was analyzed and averaged across all identified signal peaks within a defined time window (typically 1 h) centered around each peak to generate the final graph. 3D rendering of organoids growing on hydrogels with crypt-villus topology was done using Imaris 10.0 (Oxford Instruments).

To quantify apical and basal myosin levels, crypts recorded in the cross-section were selected and using FIJI a line was drawn following the shape of the epithelium with ~150 µm length. The epithelium was virtually transformed into a straight line using the *straighten* function. A line was drawn on the apical and basal surface respectively and the signal measured with a line width of 4 µm to obtain the respective line profiles. Line profiles centered around multiple crypts were

averaged and depicted in the final graph. The same approach was used to measure the apical and basal myosin profile for a single developing crypt over time. To this end, for each time point the shape of the epithelial line was adjusted and the measured distances scaled to match the length of the final crypt-villus region.

To analyze extrusion of cells upon optogenetic activation of myosin, the acquired H2B-iRFP nuclear marker signal was used to monitor cell dynamics. The detection of cell extrusion events and total cell counts were done using the FIJI plugin *Cell Counter* and the position and time were registered. Counting was done in a blinded fashion without information about the photoactivation pattern by a person, who was not the experimenter. Using Matlab, the positional and temporal data was analyzed. To analyze the extrusion rate over time, it was calculated as the average number of extrusions per total cells within a 25-minute time window. To analyze the position of extruding cells, the position data of extrusion events and total cells were binned equally using the *hist3* and visualized using the *imagesc* function. The x- and y-profile for cell extrusions and total cells was generated by calculating the mean density along the respective axis within a 9 µm window. The raw extrusion profile was then normalized by the total cell profile to obtain the final extrusion profile.

For the quantification of mosaic organoids, the respective cell population was measured as fraction of the total and extruded cell population (extrusion enrichment), extrusions and total cells were manually counted based on the co-expressed fluorescent markers using Napari and Fiji Cell counter. Counting was done in a blinded fashion. Mosaic organoids were excluded from analysis if they showed no extrusions, moved out of focus, exhibited excessive damage, or had insufficient signal strength during imaging.

Immunofluorescent staining of whole-mount intestinal tissue

Mice were sacrificed and the small intestine was dissected. The lumen was flushed several times with cold PBS. The tissue was cut as a tube and opened along the longitudinal axis. The tissue was fixed in 4% paraformaldehyde solution at 4°C overnight and washed with PBS. The cells were permeabilized using 2% PBST (2% Triton X-100 in PBS) for 2 days at room temperature and washed with PBS. The sample was incubated in blocking buffer (10% normal goat serum, 1% Triton-X 100, 2.5% DMSO in PBS) for 2 days at 4 °C. The sample was incubated in primary antibody solution (1% normal goat serum, 0.2% Triton-X 100, 2.5% DMSO, and 0.2% sodium azide in PBS; rabbit anti-Myosin light chain (phospho S20) antibody (Abcam, cat. #ab2480) diluted 1:200), incubated for 5 days at 4°C and washed with PBS at room temperature. The sample was incubated in secondary antibody solution (1:500 goat-Alexa-488-anti rabbit (Thermo Fisher Scientific, cat #A-11008) and 1:1000 phalloidin-atto647N (Sigma-Aldrich, cat. #65906)) for 2 days at 4°C and washed in PBS. The sample was stained with DAPI (1 µg/ml) diluted in PBST 4°C overnight. The sample was cleared with RapiClear 1.47 Solution (SunJin Lab, cat. #RC147001) overnight at 4°C. The sample was placed on a glass-well plate and imaged using a Leica Stellaris confocal microscope using a HC PL APO CS2 20x/0.75 air objective (Leica) for overview images (voxel size: 0.28x0.28x0.69 μm^3) and a HC PL APO CS2 63x/1.40 oil objective (Leica) for high-resolution image stacks (voxel size: 0.0586x0.0586x0.2985 μm^3). For the quantification of basal myosin level along the villus, villi that were located longitudinally to the objectives were imaged and stacks were recorded. Using Fiji, a Z-profile was generated using the *reslice* function and a line was drawn below the nuclei at the basal surface. The line profiles of several villi were overlayed relative to the distance to the villus tip.

Whole-mount organoid staining.

Organoids were fixed in 4% paraformaldehyde for 30 min at room temperature, washed in PBS, blocked in blocking solution (PBS; 0.5% Tween, 5% normal goat serum) for 1 h at room temperature and stained overnight with primary antibodies in antibody solution (PBS; 0.1% Tween, 1% normal goat serum). Primary antibody used for phosphor-Myosin-II staining: Rabbit anti-mouse phospho-myosin light chain 2 (Thr18/Ser19) (Cell Signaling Technology, cat. #3674). Primary antibody used for Epcam staining: Rat Anti-mouse CD326-APC (Clone G8.8) (eBioscience, cat. #17-5791-80). After washing in PBS, organoids were stained with secondary antibody (Goat anti-Rabbit IgG Alexa-488, Invitrogen, cat. #A-11008) in antibody solution for 1.5 h at room temperature. After washing in PBS, organoids were stained with DAPI (1 µg/ml) in PBS for 15 min and mounted on glass slides.

STED super-resolution microscopy.

Organoids were fixed in 4% paraformaldehyde for 30 min at room temperature, washed in PBS, blocked in blocking solution (PBS; 0.5% Tween, 5% normal goat serum) for 1 h at room temperature and stained overnight for phalloidin conjugated to the STED fluorophore atto647-N. The organoids were washed and incubated for 10 min at room temperature in PBS containing DAPI (1 µg/ml). Organoids were mounted in ProLong Gold Antifade Mountant (Molecular Probes/Thermo Fisher Scientific, cat. # P10144) medium on a glass carrier. A 0.16–0.19-mm-thick (thickness 1.5) cover glass (Glaswarenfabrik Karl Hecht GmbH & Co KG, cat. #41014) was placed on top, and excessive mounting medium was removed using tissue paper, dried, and sealed using nail polish. 2D-STED image stacks were collected using a Leica Stellaris 8 STED microscope with a HC PL APO CS2 100x/1.40 oil objective and type F immersion liquid. The phalloidin-atto647N–stained sample was imaged combining 650-nm excitation with the 775-nm STED

depletion laser. The image was scanned with a voxel size of 0.0199x0.0199x0.1826 µm^3, a line accumulation of 16, a dwell time of 0.75 µs. Sequentially the myosin-mNeonGreen reporter and DAPI signal was collected in the classical confocal mode.

Animal work

Mice were maintained by professional caretaker according to procedures approved by the Central Committee Animal Experimentation (CCD) of the Dutch government and approved by the KNAW/Hubrecht Institute Animal Welfare Body (IvD). Mouse strain (*Mus Musculus*): C57BL6/J, male and female of age 7-12 wks without genetic modifications (RRID:IMSR_JAX:000664) was used.

Laser ablation in the living mouse intestine.

Mice were sacrificed and immediately afterwards the intestine was dissected in ice-cold PBS-Orange containing CellMask Orange Plasma Membrane Stain (Invitrogen/Thermo Fisher Scientific, cat. #C10045) diluted 1:1000 and Primocin (InvivoGen; 1:500) in PBS. The lumen was flushed several times with ice-cold PBS-Orange. The musculature and connective tissue outside the intestinal tube was removed as much as possible. The intestine was cut open, inverted, and placed onto a glass-bottom well with a cover glass on top to bring the sample closer to the objective. The well was filled with ENR medium containing CellMask Orange (1:1000) and Primocin (1:500). A Leica SP8 confocal microscope equipped with a tunable Chameleon multiphoton laser with a HC PL IRAPO 40x/1.10 water objective (Leica) was used at room temperature and 5% CO_2. The objective was positioned at villus regions, and the cell base identified. Laser ablation using a wavelength of 800 nm of the Chameleon laser was done with a 1-pixel wide and 15 µm long line with 80 % laser intensity for 3 iterations. Before laser ablation 10 and after ablation 30 frames were

collected with a time interval of 1 s. Per mouse sample multiple positions at the villus tip and villus shaft were processed. The procedure from dissection to laser ablation was optimized to not exceed a duration of 1.5 h. To analyze tissue recoil, the Euclidean distance from the initial position was manually tracked for at least 10 cell interfaces on both sides of the ablation line. The mean recoil for each ablation experiment was calculated, and the average across multiple experiments was presented in the final graph. The initial recoil velocity was calculated by fitting a sigmoidal curve (with A: amplitude, k: steepness, t_0: inflection point, y_0: vertical offset) to each experiment and the slope of the curve at the inflection point ($v_{initial}$) was calculated:

$$f(t) = \frac{A}{1 + e^{-k(t-t_0)}} + y_0$$

$$v_{initial} = f'(t_0) = \frac{A \cdot k}{4}$$

To ablate individual cells along their apical–basal axis, villus tip regions were selected where tissue orientation allowed a ~30 µm line cut through the full length of a single cell, using the same laser settings as described above. The boundaries of the targeted cell were segmented, and all experiments were aligned by normalizing cell dimensions prior to ablation. Average cell shapes before and after ablation were calculated, and boundary displacement vectors were computed based on these contours.

To quantify orthogonal recoil upon laser ablation in crypt-villus substrates, synthetic tips were photoactivated with 488 nm light for 1 h at 5 min intervals and compared to non-activated controls. Recoil was measured by tracking H2B-iRFP–labeled nuclei along the ablation line and determining their maximal displacement within 30 s post-ablation.

Laser point ablation

For the laser point ablation experiments, organoids were seeded onto an imaging chamber (CellVis) and imaged on a Nikon A1R MP scanning confocal microscope using a 1.30 NA 40× magnification oil immersion objective, and the incubation chamber was set to (37 ºC, 5% CO_2) (*30*). For each timepoint, 31 Z-slices were imaged with 2 μm intervals. We only selected organoids that contained at least one crypt and a villus domain. An 8 ms laser stimulus of 800 nm wavelength was applied (MaiTai DeepSee, 100% laser power), which was optimized such that epithelial barrier integrity was maintained while still triggering cell extrusion. Time lapse videos for laser stimulation were acquired at more than 2 frames-per-second. Only one ablation was done per organoid and organoids were subsequently imaged for at least one hour to determine if a stimulated cell extruded. Ablated organoids were excluded from analysis if (i) the stimulus missed the organoid (i.e., if no visible bleaching of the nucleus occurred and/or no cavitation bubble was observed when stimulating the cytoskeleton), (ii) imaging failed within one hour after stimulation, (iii) ablated cells extruded to the basal side in response to the ablation. Determination of the region (base/nucleus/junction) in which cells were ablated was determined as follows: If a cavitation bubble was observed below the nucleus, a cell was classified as ablated at the base. If no cavitation bubble was observed, but the nucleus was partially bleached, the cell was classified as ablated in the nucleus. If a cavitation bubble was observed in the same xy-plane as the nucleus but a cavitation bubble was observed outside the nucleus, the stimulation was classified as a stimulation of a multicellular junction. Whether cells extruded (within 1 hour) in response to point ablation was determined by visual inspection. To determine the extrusion time of cells that extruded in response to the point ablation, we tracked the nuclei of the extruding cells and their immediate neighbors for 1 hour. For single-cellular extrusions, we computed the relative vertical displacement of the extruding cells from their non-extruding neighbors (ΔZ) as follows:

$$\Delta Z = Z_i - \frac{1}{|\Omega_i|}\sum_{j\in\Omega_i} Z_j$$

Where Ω_i is the set of neighbors of extruding cell i. For multicellular extrusions, we computed ΔZ as:

$$\Delta Z = \bar{Z}_{ext} - \frac{1}{|\Omega|}\sum_{j\in\Omega} Z_j$$

Where $\bar{Z}_{ext}$ is the average Z-level of all the co-extruding cells, and Ω is the set of all non-extruding neighbors of all extruding cells. Extrusion time was defined as the time until $\Delta Z > 5$ µm.

Real-Time quantitative PCR

Total RNA was extracted from control and *Epcam*$^{-/-}$ organoids using the RNeasy Mini Kit (Quiagen), following the manufacturer's protocol. RNA concentration was determined spectrophotometrically and diluted to a uniform concentration. cDNA was synthesized from 540 ng total RNA using the High-Capacity RNA-to-cDNA™ Kit (Applied Biosystems, cat. #4388950). Quantitative PCR was performed using SYBR Green Supermix (Bio-Rad, cat. #1725121) in 384-well format with gene-specific primers (**Table S2**) and 4 ng of cDNA per reaction. The cycling protocol consisted of an initial denaturation at 95 °C for 3 min, followed by 40 cycles of 95 °C for 10 s, 60 °C for 30 s, and 72 °C for 30 s. Fluorescence was recorded after each cycle. Average CT values were calculated from technical duplicates and normalized to the geometric mean of *Actb* and *Gapdh*. Relative gene expression levels were determined using the ΔΔCT method and normalized to control organoids.

Pharmacological treatments

For the laser ablation of blebbistatin-treated organoids, the organoids were incubated overnight in ENR medium supplemented with 100 µM (±)-blebbistatin (Abcam, cat. #120425). For measuring

extrusions in mosaic *EPCAM*$^{-/-}$ organoids, organoids were pre-incubated for 5 h in 50 µM Y-16 (MedChemExpress, cat. #HY-12649) and 10 µM Y27632 (AbMole, cat. #M1817) and imaged for 16 h.

Statistical analysis

Statistical tests were done using the scipy.stats library (*85*) and the Matlab *Statistics and Machine Learning Toolbox* (Mathworks).

References and Notes

1. A. S. Darwich, U. Aslam, D. M. Ashcroft, A. Rostami-Hodjegan, Meta-Analysis of the Turnover of Intestinal Epithelia in Preclinical Animal Species and Humans. *Drug Metab Dispos* **42**, 2016–2022 (2014).

2. N. Barker, Adult intestinal stem cells: critical drivers of epithelial homeostasis and regeneration. *Nat Rev Mol Cell Biol* **15**, 19–33 (2014).

3. D. Krndija, F. El Marjou, B. Guirao, S. Richon, O. Leroy, Y. Bellaiche, E. Hannezo, D. Matic Vignjevic, Active cell migration is critical for steady-state epithelial turnover in the gut. *Science* **365**, 705–710 (2019).

4. A. G. Schepers, R. Vries, M. van den Born, M. van de Wetering, H. Clevers, Lgr5 intestinal stem cells have high telomerase activity and randomly segregate their chromosomes: Lgr5 adult intestinal stem cell characteristics. *The EMBO Journal* **30**, 1104–1109 (2011).

5. N. Barker, J. H. van Es, J. Kuipers, P. Kujala, M. van den Born, M. Cozijnsen, A. Haegebarth, J. Korving, H. Begthel, P. J. Peters, H. Clevers, Identification of stem cells in small intestine and colon by marker gene Lgr5. *Nature* **449**, 1003–1007 (2007).

6. T. Sato, R. G. Vries, H. J. Snippert, M. van de Wetering, N. Barker, D. E. Stange, J. H. van Es, A. Abo, P. Kujala, P. J. Peters, H. Clevers, Single Lgr5 stem cells build crypt-villus structures in vitro without a mesenchymal niche. *Nature* **459**, 262–265 (2009).

7. T. Sato, J. H. van Es, H. J. Snippert, D. E. Stange, R. G. Vries, M. van den Born, N. Barker, N. F. Shroyer, M. van de Wetering, H. Clevers, Paneth cells constitute the niche for Lgr5 stem cells in intestinal crypts. *Nature* **469**, 415–418 (2011).

8. N. Gjorevski, M. Nikolaev, T. E. Brown, O. Mitrofanova, N. Brandenberg, F. W. DelRio, F. M. Yavitt, P. Liberali, K. S. Anseth, M. P. Lutolf, Tissue geometry drives deterministic organoid patterning. *Science* **375**, eaaw9021 (2022).

9. T. Cumming, R. Levayer, Toward a predictive understanding of epithelial cell death. *Seminars in Cell & Developmental Biology* **156**, 44–57 (2024).

10. X. Ai, D. Wang, J. Zhang, J. Shen, Hippo signaling promotes Ets21c-dependent apical cell extrusion in the *Drosophila* wing disc. *Development*, dev.190124 (2020).

11. Y. Gu, T. Forostyan, R. Sabbadini, J. Rosenblatt, Epithelial cell extrusion requires the sphingosine-1-phosphate receptor 2 pathway. *Journal of Cell Biology* **193**, 667–676 (2011).

12. K. Duszyc, G. A. Gomez, A. K. Lagendijk, M.-K. Yau, B. N. Nanavati, B. L. Gliddon, T. E. Hall, S. Verma, B. M. Hogan, S. M. Pitson, D. P. Fairlie, R. G. Parton, A. S. Yap, Mechanotransduction activates RhoA in the neighbors of apoptotic epithelial cells to engage apical extrusion. *Current Biology* **31**, 1326-1336.e5 (2021).

13. D. M. Pritchard, C. S. Potten, S. J. Korsmeyer, S. Roberts, J. A. Hickman, Damage-induced apoptosis in intestinal epithelia from bcl-2-null and bax-null mice: investigations of the mechanistic determinants of epithelial apoptosis in vivo. *Oncogene* **18**, 7287–7293 (1999).

14. D. M. Pritchard, C. Print, L. O'Reilly, J. M. Adams, C. S. Potten, J. A. Hickman, Bcl-w is an important determinant of damage-induced apoptosis in epithelia of small and large intestine. *Oncogene* **19**, 3955–3959 (2000).

15. C. Günther, E. Martini, N. Wittkopf, K. Amann, B. Weigmann, H. Neumann, M. J. Waldner, S. M. Hedrick, S. Tenzer, M. F. Neurath, C. Becker, Caspase-8 regulates TNF-α-induced epithelial necroptosis and terminal ileitis. *Nature* **477**, 335–339 (2011).

16. F. Ghazavi, J. Huysentruyt, J. De Coninck, S. Kourula, S. Martens, B. Hassannia, T. Wartewig, T. Divert, R. Roelandt, B. Popper, A. Hiergeist, P. Tougaard, T. Vanden Berghe, M. Joossens, G. Berx, N. Takahashi, A. Wahida, P. Vandenabeele, Executioner caspases 3 and 7 are dispensable for intestinal epithelium turnover and homeostasis at steady state. *Proc. Natl. Acad. Sci. U.S.A.* **119**, e2024508119 (2022).

17. G. T. Eisenhoffer, P. D. Loftus, M. Yoshigi, H. Otsuna, C.-B. Chien, P. A. Morcos, J. Rosenblatt, Crowding induces live cell extrusion to maintain homeostatic cell numbers in epithelia. *Nature* **484**, 546–549 (2012).

18. E. Marinari, A. Mehonic, S. Curran, J. Gale, T. Duke, B. Baum, Live-cell delamination counterbalances epithelial growth to limit tissue overcrowding. *Nature* **484**, 542–545 (2012).

19. R. Levayer, C. Dupont, E. Moreno, Tissue Crowding Induces Caspase-Dependent Competition for Space. *Current Biology* **26**, 670–677 (2016).

20. C. Pérez-González, G. Ceada, M. Matejčić, X. Trepat, Digesting the mechanobiology of the intestinal epithelium. *Current Opinion in Genetics & Development* **72**, 82–90 (2022).

21. R. M. Houtekamer, M. C. Van Der Net, M. M. Maurice, M. Gloerich, Mechanical forces directing intestinal form and function. *Current Biology* **32**, R791–R805 (2022).

22. T. F. Bullen, S. Forrest, F. Campbell, A. R. Dodson, M. J. Hershman, D. M. Pritchard, J. R. Turner, M. H. Montrose, A. J. M. Watson, Characterization of epithelial cell shedding from human small intestine. *Laboratory Investigation* **86**, 1052–1063 (2006).

23. J. M. Williams, C. A. Duckworth, A. J. M. Watson, M. R. Frey, J. C. Miguel, M. D. Burkitt, R. Sutton, K. R. Hughes, L. J. Hall, J. H. Caamaño, B. J. Campbell, D. M. Pritchard, A mouse model of pathological small intestinal epithelial cell apoptosis and shedding induced by systemic administration of lipopolysaccharide. *Disease Models & Mechanisms*, dmm.013284 (2013).

24. Y. Atieh, T. Wyatt, A. M. Zaske, G. T. Eisenhoffer, Pulsatile contractions promote apoptotic cell extrusion in epithelial tissues. *Current Biology* **31**, 1129-1140.e4 (2021).

25. T. Zulueta-Coarasa, J. Rosenblatt, The role of tissue maturity and mechanical state in controlling cell extrusion. *Current Opinion in Genetics & Development* **72**, 1–7 (2022).

26. S. Curran, C. Strandkvist, J. Bathmann, M. De Gennes, A. Kabla, G. Salbreux, B. Baum, Myosin II Controls Junction Fluctuations to Guide Epithelial Tissue Ordering. *Developmental Cell* **43**, 480-492.e6 (2017).

27. M. Michel, C. Dahmann, Tissue mechanical properties modulate cell extrusion in the *Drosophila* abdominal epidermis. *Development* **147**, dev179606 (2020).

28. J. L. Teo, G. A. Gomez, S. Weeratunga, E. M. Davies, I. Noordstra, S. Budnar, H. Katsuno-Kambe, M. J. McGrath, S. Verma, V. Tomatis, B. R. Acharya, L. Balasubramaniam, R. M. Templin, K.-A. McMahon, Y. S. Lee, R. J. Ju, S. J. Stebhens, B. Ladoux, C. A. Mitchell, B. M. Collins, R. G. Parton, A. S. Yap, Caveolae Control Contractile Tension for Epithelia to Eliminate Tumor Cells. *Developmental Cell* **54**, 75-91.e7 (2020).

29. R. N. U. Kok, L. Hebert, G. Huelsz-Prince, Y. J. Goos, X. Zheng, K. Bozek, G. J. Stephens, S. J. Tans, J. S. van Zon, OrganoidTracker: Efficient cell tracking using machine learning and manual error correction. *PLoS ONE* **15**, e0240802 (2020).

30. G. Huelsz-Prince, R. N. U. Kok, Y. Goos, L. Bruens, X. Zheng, S. Ellenbroek, J. Van Rheenen, S. Tans, J. S. van Zon, Mother cells control daughter cell proliferation in intestinal organoids to minimize proliferation fluctuations. *eLife* **11**, e80682 (2022).

31. M. S. Levine, A. J. Holland, The impact of mitotic errors on cell proliferation and tumorigenesis. *Genes Dev.* **32**, 620–638 (2018).

32. I. Bonnet, P. Marcq, F. Bosveld, L. Fetler, Y. Bellaïche, F. Graner, Mechanical state, material properties and continuous description of an epithelial tissue. *J. R. Soc. Interface.* **9**, 2614–2623 (2012).

33. Q. Yang, S.-L. Xue, C. J. Chan, M. Rempfler, D. Vischi, F. Maurer-Gutierrez, T. Hiiragi, E. Hannezo, P. Liberali, Cell fate coordinates mechano-osmotic forces in intestinal crypt formation. *Nat Cell Biol* **23**, 733–744 (2021).

34. C. Pérez-González, G. Ceada, F. Greco, M. Matejčić, M. Gómez-González, N. Castro, A. Menendez, S. Kale, D. Krndija, A. G. Clark, V. R. Gannavarapu, A. Álvarez-Varela, P. Roca-Cusachs, E. Batlle, D. M. Vignjevic, M. Arroyo, X. Trepat, Mechanical compartmentalization of the intestinal organoid enables crypt folding and collective cell migration. *Nat Cell Biol* **23**, 745–757 (2021).

35. A. Popkova, O. J. Stone, L. Chen, X. Qin, C. Liu, J. Liu, K. Belguise, D. J. Montell, K. M. Hahn, M. Rauzi, X. Wang, A Cdc42-mediated supracellular network drives polarized forces and Drosophila egg chamber extension. *Nat Commun* **11**, 1921 (2020).

36. M. Behrndt, G. Salbreux, P. Campinho, R. Hauschild, F. Oswald, J. Roensch, S. W. Grill, C.-P. Heisenberg, Forces Driving Epithelial Spreading in Zebrafish Gastrulation. *Science* **338**, 257–260 (2012).

37. A. C. Martin, M. Kaschube, E. F. Wieschaus, Pulsed contractions of an actin–myosin network drive apical constriction. *Nature* **457**, 495–499 (2009).

38. A. Sutherland, A. Lesko, Pulsed actomyosin contractions in morphogenesis. *F1000Res* **9**, 142 (2020).

39. Y. An, G. Xue, Y. Shaobo, D. Mingxi, X. Zhou, W. Yu, T. Ishibashi, L. Zhang, Y. Yan, Apical constriction is driven by a pulsatile apical myosin network in delaminating Drosophila neuroblasts. *Development*, dev.150763 (2017).

40. S. Chanet, C. J. Miller, E. D. Vaishnav, B. Ermentrout, L. A. Davidson, A. C. Martin, Actomyosin meshwork mechanosensing enables tissue shape to orient cell force. *Nat Commun* **8**, 15014 (2017).

41. L. Valon, A. Marín-Llauradó, T. Wyatt, G. Charras, X. Trepat, Optogenetic control of cellular forces and mechanotransduction. *Nat Commun* **8**, 14396 (2017).

42. T. Matsushita, H. Hayashi, S. Kunishima, M. Hayashi, M. Ikejiri, K. Takeshita, Y. Yuzawa, T. Adachi, K. Hirashima, M. Sone, K. Yamamoto, A. Takagi, A. Katsumi, K. Kawai, T. Nezu, M. Takahashi, T. Nakashima, T. Naoe, T. Kojima, H. Saito, Targeted disruption of mouse ortholog of the human MYH9 responsible for macrothrombocytopenia with different organ involvement: hematological, nephrological, and otological studies of heterozygous KO mice. *Biochemical and Biophysical Research Communications* **325**, 1163–1171 (2004).

43. Y. Zhang, M. A. Conti, D. Malide, F. Dong, A. Wang, Y. A. Shmist, C. Liu, P. Zerfas, M. P. Daniels, C.-C. Chan, E. Kozin, B. Kachar, M. J. Kelley, J. B. Kopp, R. S. Adelstein, Mouse models of MYH9-related disease: mutations in nonmuscle myosin II-A. *Blood* **119**, 238–250 (2012).

44. M. F. Schliffka, A. F. Tortorelli, Ö. Özgüç, L. De Plater, O. Polzer, D. Pelzer, J.-L. Maître, Multiscale analysis of single and double maternal-zygotic Myh9 and Myh10 mutants during mouse preimplantation development. *eLife* **10**, e68536 (2021).

45. J.-L. Maître, H. Turlier, R. Illukkumbura, B. Eismann, R. Niwayama, F. Nédélec, T. Hiiragi, Asymmetric division of contractile domains couples cell positioning and fate specification. *Nature* **536**, 344–348 (2016).

46. M. Rauzi, P. Verant, T. Lecuit, P.-F. Lenne, Nature and anisotropy of cortical forces orienting Drosophila tissue morphogenesis. *Nat Cell Biol* **10**, 1401–1410 (2008).

47. M. Sivagnanam, J. L. Mueller, H. Lee, Z. Chen, S. F. Nelson, D. Turner, S. H. Zlotkin, P. B. Pencharz, B. Ngan, O. Libiger, N. J. Schork, J. E. Lavine, S. Taylor, R. O. Newbury, R. D. Kolodner, H. M. Hoffman, Identification of EpCAM as the Gene for Congenital Tufting Enteropathy. *Gastroenterology* **135**, 429–437 (2008).

48. J. L. Mueller, M. D. McGeough, C. A. Peña, M. Sivagnanam, Functional consequences of *EpCam* mutation in mice and men. *American Journal of Physiology-Gastrointestinal and Liver Physiology* **306**, G278–G288 (2014).

49. N. Maghzal, H. A. Kayali, N. Rohani, A. V. Kajava, F. Fagotto, EpCAM Controls Actomyosin Contractility and Cell Adhesion by Direct Inhibition of PKC. *Developmental Cell* **27**, 263–277 (2013).

50. T. Ouchi, S. Morimura, L. E. Dow, H. Miyoshi, M. C. Udey, EpCAM (CD326) Regulates Intestinal Epithelial Integrity and Stem Cells via Rho-Associated Kinase. *Cells* **10**, 256 (2021).

51. B. Das, M. Sivagnanam, Congenital Tufting Enteropathy: Biology, Pathogenesis and Mechanisms. *JCM* **10**, 19 (2020).

52. B. Das, K. Okamoto, J. Rabalais, J. A. Young, K. E. Barrett, M. Sivagnanam, Aberrant Epithelial Differentiation Contributes to Pathogenesis in a Murine Model of Congenital Tufting Enteropathy. *Cellular and Molecular Gastroenterology and Hepatology* **12**, 1353–1371 (2021).

53. B. Das, K. Okamoto, J. Rabalais, P. A. Kozan, R. R. Marchelletta, M. D. McGeough, N. Durali, M. Go, K. E. Barrett, S. Das, M. Sivagnanam, Enteroids expressing a disease-associated mutant of EpCAM are a model for congenital tufting enteropathy. *American Journal of Physiology-Gastrointestinal and Liver Physiology* **317**, G580–G591 (2019).

54. F. Meng, C. Shen, L. Yang, C. Ni, J. Huang, K. Lin, Z. Cao, S. Xu, W. Cui, X. Wang, B. Zhou, C. Xiong, J. Wang, B. Zhao, Mechanical stretching boosts expansion and regeneration of intestinal organoids through fueling stem cell self-renewal. *Cell Regen* **11**, 39 (2022).

55. M. B. Baghdadi, R. M. Houtekamer, L. Perrin, A. Rao-Bhatia, M. Whelen, L. Decker, M. Bergert, C. Pérez-Gonzàlez, R. Bouras, G. Gropplero, A. K. H. Loe, A. Afkhami-Poostchi, X. Chen, X. Huang, S. Descroix, J. L. Wrana, A. Diz-Muñoz, M. Gloerich, A. Ayyaz, D. Matic Vignjevic, T.-H. Kim, PIEZO-dependent mechanosensing is essential for intestinal stem cell fate decision and maintenance. *Science* **386**, eadj7615 (2024).

56. S. A. Gudipaty, J. Lindblom, P. D. Loftus, M. J. Redd, K. Edes, C. F. Davey, V. Krishnegowda, J. Rosenblatt, Mechanical stretch triggers rapid epithelial cell division through Piezo1. *Nature* **543**, 118–121 (2017).

57. M. E. Fernández-Sánchez, S. Barbier, J. Whitehead, G. Béalle, A. Michel, H. Latorre-Ossa, C. Rey, L. Fouassier, A. Claperon, L. Brullé, E. Girard, N. Servant, T. Rio-Frio, H. Marie, S. Lesieur, C. Housset, J.-L. Gennisson, M. Tanter, C. Ménager, S. Fre, S. Robine, E. Farge, Mechanical induction of the tumorigenic β-catenin pathway by tumour growth pressure. *Nature* **523**, 92–95 (2015).

58. A. U. Spencer, X. Sun, M. El-Sawaf, E. Q. Haxhija, D. Brei, J. Luntz, H. Yang, D. H. Teitelbaum, Enterogenesis in a clinically feasible model of mechanical small-bowel lengthening. *Surgery* **140**, 212–220 (2006).

59. H. A. Messal, S. Alt, R. M. M. Ferreira, C. Gribben, V. M.-Y. Wang, C. G. Cotoi, G. Salbreux, A. Behrens, Tissue curvature and apicobasal mechanical tension imbalance instruct cancer morphogenesis. *Nature* **566**, 126–130 (2019).

60. L. Sui, S. Alt, M. Weigert, N. Dye, S. Eaton, F. Jug, E. W. Myers, F. Jülicher, G. Salbreux, C. Dahmann, Differential lateral and basal tension drive folding of Drosophila wing discs through two distinct mechanisms. *Nat Commun* **9**, 4620 (2018).

61. R. Priya, S. Allanki, A. Gentile, S. Mansingh, V. Uribe, H.-M. Maischein, D. Y. R. Stainier, Tension heterogeneity directs form and fate to pattern the myocardial wall. *Nature* **588**, 130–134 (2020).

62. N. G. Naydenov, A. Feygin, D. Wang, J. F. Kuemmerle, G. Harris, M. A. Conti, R. S. Adelstein, A. I. Ivanov, Nonmuscle Myosin IIA Regulates Intestinal Epithelial Barrier in vivo and Plays a Protective Role During Experimental Colitis. *Sci Rep* **6**, 24161 (2016).

63. L. D. C. Martínez-Sánchez, P. A. Ngo, R. Pradhan, L.-S. Becker, D. Boehringer, D. Soteriou, M. Kubankova, C. Schweitzer, T. Koch, V. Thonn, L. Erkert, I. Stolzer, C. Günther, C. Becker, B. Weigmann, M. Klewer, C. Daniel, K. Amann, S. Tenzer, R. Atreya, M. Bergo, C. Brakebusch, A. J. M. Watson, J. Guck, B. Fabry, I. Atreya, M. F. Neurath, R. López-Posadas, Epithelial RAC1-dependent cytoskeleton dynamics controls cell mechanics, cell shedding and barrier integrity in intestinal inflammation. *Gut* **72**, 275–294 (2023).

64. A. A. van Bodegraven, C. R. Curley, K. A. Hunt, A. J. Monsuur, R. K. Linskens, C. M. Onnie, J. B. A. Crusius, V. Annese, A. Latiano, M. S. Silverberg, A. Bitton, S. A. Fisher, A. H. Steinhart, A. Forbes, J. Sanderson, N. J. Prescott, D. P. Strachan, R. J. Playford, C. G. Mathew, C. Wijmenga, M. J. Daly, J. D. Rioux, D. A. van Heel, Genetic Variation in Myosin IXB Is Associated With Ulcerative Colitis. *Gastroenterology* **131**, 1768–1774 (2006).

65. H. Baribault, J. Penner, R. V. Iozzo, M. Wilson-Heiner, Colorectal hyperplasia and inflammation in keratin 8-deficient FVB/N mice. *Genes Dev.* **8**, 2964–2973 (1994).

66. Y. Ma, J. Yue, Y. Zhang, C. Shi, M. Odenwald, W. G. Liang, Q. Wei, A. Goel, X. Gou, J. Zhang, S.-Y. Chen, W.-J. Tang, J. R. Turner, F. Yang, H. Liang, H. Qin, X. Wu, ACF7 regulates inflammatory colitis and intestinal wound response by orchestrating tight junction dynamics. *Nat Commun* **8**, 15375 (2017).

67. G. M. Slattum, J. Rosenblatt, Tumour cell invasion: an emerging role for basal epithelial cell extrusion. *Nat Rev Cancer* **14**, 495–501 (2014).

68. T. W. Marshall, I. E. Lloyd, J. M. Delalande, I. Näthke, J. Rosenblatt, The tumor suppressor adenomatous polyposis coli controls the direction in which a cell extrudes from an epithelium. *MBoC* **22**, 3962–3970 (2011).

69. U. A. Hänninen, R. Katainen, T. Tanskanen, R.-M. Plaketti, R. Laine, J. Hamberg, A. Ristimäki, E. Pukkala, M. Taipale, J.-P. Mecklin, L. M. Forsström, E. Pitkänen, K. Palin, N. Välimäki, N. Mäkinen, L. A. Aaltonen, Exome-wide somatic mutation characterization of small bowel adenocarcinoma. *PLoS Genet* **14**, e1007200 (2018).

70. A. Nyga, S. Ganguli, H. K. Matthews, B. Baum, The role of RAS oncogenes in controlling epithelial mechanics. *Trends in Cell Biology* **33**, 60–69 (2023).

71. D. S. Bryan, M. Stack, K. Krysztofiak, U. Cichoń, D. G. Thomas, A. Surcel, E. S. Schiffhauer, M. A. Beckett, N. N. Khodarev, L. Xue, E. C. Poli, A. T. Pearson, M. C. Posner, D. N. Robinson, R. S. Rock, R. R. Weichselbaum, 4-Hydroxyacetophenone modulates the actomyosin cytoskeleton to reduce metastasis. *Proc. Natl. Acad. Sci. U.S.A.* **117**, 22423–22429 (2020).

72. P. Muenzner, M. Rohde, S. Kneitz, C. R. Hauck, CEACAM engagement by human pathogens enhances cell adhesion and counteracts bacteria-induced detachment of epithelial cells. *The Journal of Cell Biology* **170**, 825–836 (2005).

73. M. Kim, M. Ogawa, Y. Fujita, Y. Yoshikawa, T. Nagai, T. Koyama, S. Nagai, A. Lange, R. Fässler, C. Sasakawa, Bacteria hijack integrin-linked kinase to stabilize focal adhesions and block cell detachment. *Nature* **459**, 578–582 (2009).

74. A. C. Fasciano, G. S. Dasanayake, M. K. Estes, N. C. Zachos, D. T. Breault, R. R. Isberg, S. Tan, J. Mecsas, Yersinia pseudotuberculosis YopE prevents uptake by M cells and instigates M cell extrusion in human ileal enteroid-derived monolayers. *Gut Microbes* **13**, 1988390 (2021).

75. C. Pleguezuelos-Manzano, J. Puschhof, S. Van Den Brink, V. Geurts, J. Beumer, H. Clevers, Establishment and Culture of Human Intestinal Organoids Derived from Adult Stem Cells. *CP in Immunology* **130**, e106 (2020).

76. E. Izquierdo, T. Quinkler, S. De Renzis, Guided morphogenesis through optogenetic activation of Rho signalling during early Drosophila embryogenesis. *Nat Commun* **9**, 2366 (2018).

77. J. Beumer, J. Puschhof, J. Bauzá-Martinez, A. Martínez-Silgado, R. Elmentaite, K. R. James, A. Ross, D. Hendriks, B. Artegiani, G. A. Busslinger, B. Ponsioen, A. Andersson-Rolf, A. Saftien, C. Boot, K. Kretzschmar, M. H. Geurts, Y. E. Bar-Ephraim, C. Pleguezuelos-Manzano, Y. Post, H. Begthel, F. Van Der Linden, C. Lopez-Iglesias, W. J. Van De Wetering, R. Van Der Linden, P. J. Peters, A. J. R. Heck, J. Goedhart, H. Snippert, M. Zilbauer, S. A. Teichmann, W. Wu, H. Clevers, High-Resolution mRNA and Secretome Atlas of Human Enteroendocrine Cells. *Cell* **181**, 1291-1306.e19 (2020).

78. J. L. Schmid-Burgk, K. Höning, T. S. Ebert, V. Hornung, CRISPaint allows modular base-specific gene tagging using a ligase-4-dependent mechanism. *Nat Commun* **7**, 12338 (2016).

79. B. Artegiani, D. Hendriks, J. Beumer, R. Kok, X. Zheng, I. Joore, S. Chuva de Sousa Lopes, J. van Zon, S. Tans, H. Clevers, Fast and efficient generation of knock-in human organoids using homology-independent CRISPR–Cas9 precision genome editing. *Nat Cell Biol* **22**, 321–331 (2020).

80. M. Fujii, M. Matano, K. Nanki, T. Sato, Efficient genetic engineering of human intestinal organoids using electroporation. *Nat Protoc* **10**, 1474–1485 (2015).

81. X. Zheng, M. A. Betjes, P. Ender, Y. J. Goos, G. Huelsz-Prince, H. Clevers, J. S. Van Zon, S. J. Tans, Organoid cell fate dynamics in space and time. *Sci. Adv.* **9**, eadd6480 (2023).

82. J. Schindelin, I. Arganda-Carreras, E. Frise, V. Kaynig, M. Longair, T. Pietzsch, S. Preibisch, C. Rueden, S. Saalfeld, B. Schmid, J.-Y. Tinevez, D. J. White, V. Hartenstein, K. Eliceiri, P. Tomancak, A. Cardona, Fiji: an open-source platform for biological-image analysis. *Nat Methods* **9**, 676–682 (2012).

83. C. T. Rueden, J. Schindelin, M. C. Hiner, B. E. DeZonia, A. E. Walter, E. T. Arena, K. W. Eliceiri, ImageJ2: ImageJ for the next generation of scientific image data. *BMC Bioinformatics* **18**, 529 (2017).

84. S. Herbert, L. Valon, L. Mancini, N. Dray, P. Caldarelli, J. Gros, E. Esposito, S. L. Shorte, L. Bally-Cuif, N. Aulner, R. Levayer, J.-Y. Tinevez, LocalZProjector and DeProj: a toolbox for local 2D projection and accurate morphometrics of large 3D microscopy images. *BMC Biol* **19**, 136 (2021).

85. P. Virtanen, R. Gommers, T. E. Oliphant, M. Haberland, T. Reddy, D. Cournapeau, E. Burovski, P. Peterson, W. Weckesser, J. Bright, S. J. van der Walt, M. Brett, J. Wilson, K. J. Millman, N. Mayorov, A. R. J. Nelson, E. Jones, R. Kern, E. Larson, C. J. Carey, İ. Polat, Y. Feng, E. W. Moore, J. VanderPlas, D. Laxalde, J. Perktold, R. Cimrman, I. Henriksen, E. A. Quintero, C. R. Harris, A. M. Archibald, A. H. Ribeiro, F. Pedregosa, P. van Mulbregt, SciPy 1.0 Contributors, A. Vijaykumar, A. P. Bardelli, A. Rothberg, A. Hilboll, A. Kloeckner, A. Scopatz, A. Lee, A. Rokem, C. N. Woods, C. Fulton, C. Masson, C. Häggström, C. Fitzgerald, D. A. Nicholson, D. R. Hagen, D. V. Pasechnik, E. Olivetti, E. Martin, E. Wieser, F. Silva, F. Lenders, F. Wilhelm, G. Young, G. A. Price, G.-L. Ingold, G. E. Allen, G. R. Lee, H. Audren, I. Probst, J. P. Dietrich, J. Silterra, J. T. Webber, J. Slavič, J. Nothman, J. Buchner, J. Kulick, J. L. Schönberger, J. V. de Miranda Cardoso, J. Reimer, J. Harrington, J. L. C. Rodríguez, J. Nunez-Iglesias, J. Kuczynski, K. Tritz, M. Thoma, M. Newville, M. Kümmerer, M. Bolingbroke, M. Tartre, M. Pak, N. J. Smith, N. Nowaczyk, N. Shebanov, O. Pavlyk, P. A. Brodtkorb, P. Lee, R. T. McGibbon, R. Feldbauer, S. Lewis, S. Tygier, S. Sievert, S. Vigna, S. Peterson, S. More, T. Pudlik, T. Oshima, T. J. Pingel, T. P. Robitaille, T. Spura, T. R. Jones, T. Cera, T. Leslie, T. Zito, T. Krauss, U. Upadhyay, Y. O. Halchenko, Y. Vázquez-Baeza, SciPy 1.0: fundamental algorithms for scientific computing in Python. *Nat Methods* **17**, 261–272 (2020).

Acknowledgments:

We thank Marco Kamp for assistance and maintenance of the imaging setups at AMOLF, Yvonne Goos for lab management, Guizela Huelsz-Prince, Xuan Zheng, Max Betjes, Pascal Ender, Michael Vennettilli, Pieter Rein ten Wolde and all members of the Tans, van Zon, and Clevers laboratories for helpful discussion. We thank Katharina Sonnen and Sonja Wetering for kindly sharing equipment, technical support, and helpful discussions. We thank Anko de Graaf and the Hubrecht imaging center for the maintenance of equipment.

Funding:

Dutch Research Council, NWO Building Blocks of Life grant, number 737.016.009 (RK, JVZ, SJT)

Dutch Research Council, NWO Groot grant, number 2019.085 (WKS, JVZ, SJT, HC)

Netherlands Organization for Scientific Research, Gravitation Program "Materials Driven Regeneration", number 024.003.013 (DK, JVE, HC)

European Commission, H2020-MSCA-IF-2020, MCExtrusion number 101026478 (DK)

Author contributions:

Conceptualization: DK, WKS, JVE, JVZ, SJT, HC

Methodology: DK, WKS, MN, NG, ML, JVE, DJM, SW

Investigation: DK, WKS, RK, DJM, SW, MBH

Visualization: DK, WKS, RK

Funding acquisition: DK, JVE, JVZ, SJT, HC

Software: RK, JVZ, WKS

Project administration: DK, WKS, JVE, JVZ, SJT, HC

Supervision: JVE, JVZ, SJT, HC

Writing – original draft: DK, WKS

Writing – review & editing: DK, WKS, JVZ, SJT, HC

Competing interests:

H.C. is head of Pharma Research and Early Development (pRED) at Roche. H.C. is inventor of several patents related to organoid technology; his full disclosure is given at https://www.uu.nl/staff/JCClevers/AncillaryActivities. M.N., M.P.L., and N.G. are named as inventors on patents (EP16199677.2, PCT/EP2017/079651, US20190367872A1) related to the scaffold-guided organoid technology used in this study.

Data and materials availability:

All data are available in the manuscript or the supplementary materials. Plasmids are available at Addgene.

Supplementary Materials

Figs. S1 to S9

Table S1 to S2

Movies S1 to S11

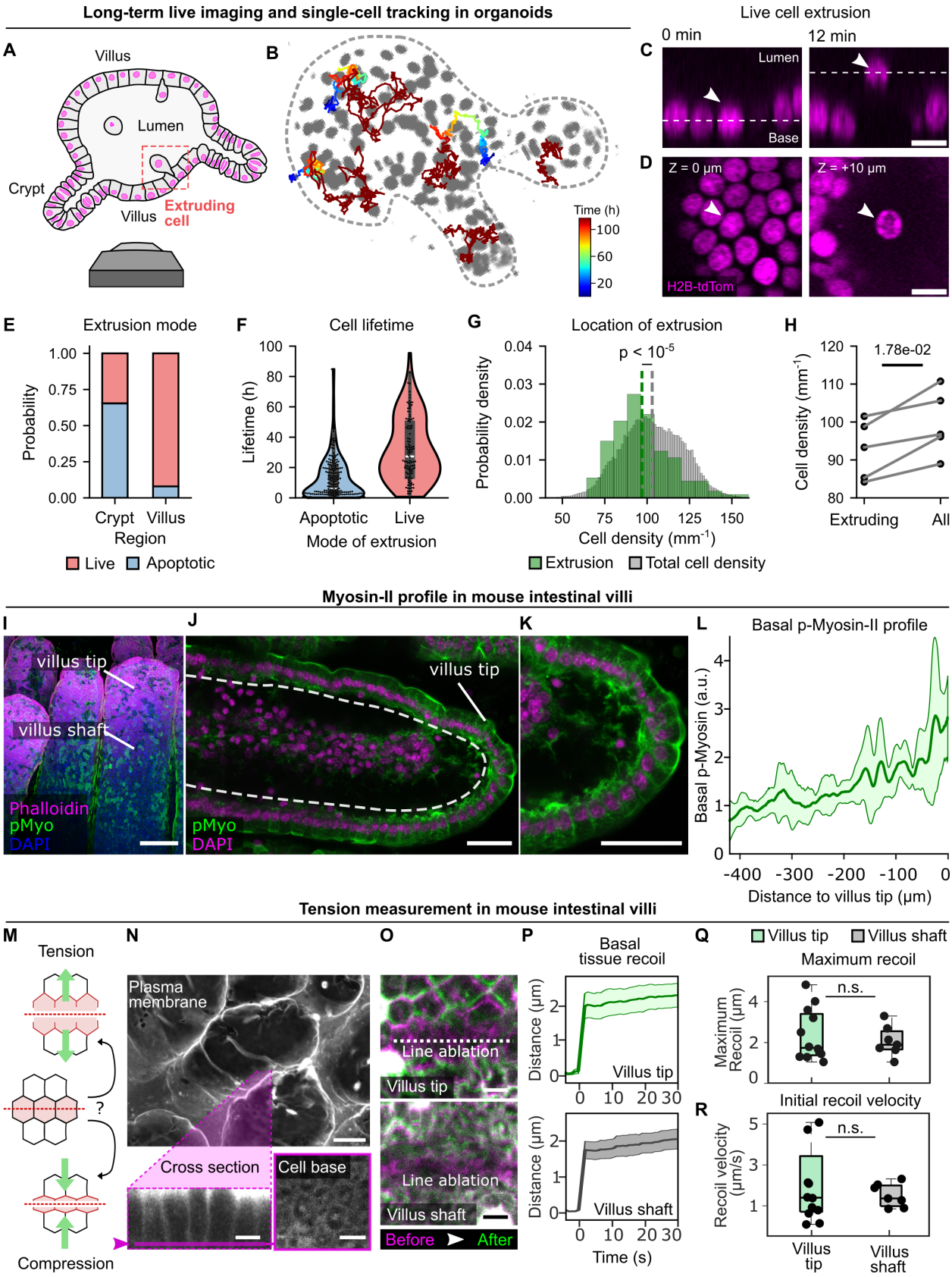
Long-term live imaging and single-cell tracking in organoids
A
Villus
Lumen
Crypt
Villus
Extruding cell
B
Time (h)
100
60
20
Live cell extrusion
C
0 min
12 min
Lumen
Base
D
Z = 0 µm
Z = +10 µm
H2B-tdTom
E
Extrusion mode
Probability
1.00
0.75
0.50
0.25
0.00
Crypt
Villus
Region
Live
Apoptotic
F
Cell lifetime
Lifetime (h)
100
80
60
40
20
0
Apoptotic
Live
Mode of extrusion
G
Location of extrusion
p < 10-5
Probability density
0.04
0.03
0.02
0.01
0.00
50
75
100
125
150
Cell density (mm-1)
Extrusion
Total cell density
H
1.78e-02
Cell density (mm-1)
120
110
100
90
80
Extruding
All
Myosin-II profile in mouse intestinal villi
I
villus tip
villus shaft
Phalloidin
pMyo
DAPI
J
villus tip
pMyo
DAPI
K
L
Basal p-Myosin-II profile
Basal p-Myosin (a.u.)
4
3
2
1
0
-400
-300
-200
-100
0
Distance to villus tip (µm)
Tension measurement in mouse intestinal villi
M
Tension
?
Compression
N
Plasma membrane
Cross section
Cell base
O
Line ablation
Villus tip
Line ablation
Villus shaft
Before
After
P
Basal tissue recoil
Distance (µm)
2
1
0
Villus tip
0
10
20
30
Distance (µm)
2
1
0
Villus shaft
0
10
20
30
Time (s)
Q
Villus tip
Villus shaft
Maximum recoil
Maximum Recoil (µm)
4
2
0
n.s.
R
Initial recoil velocity
Recoil velocity (µm/s)
5
3
1
n.s.
Villus tip
Villus shaft

Fig. 1. Intestinal live-cell extrusion occurs predominantly from regions under tension. (A) Live imaging and single-cell tracking of nuclear-labeled intestinal organoids. **(B)** Time-colored tracks overlaid on a tracked organoid. **(C, D)** Cross-section **(C)** and top-view **(D)** of a live-cell extrusion, defined by the presence of an unfragmented nucleus at its final timepoint in the epithelium. Arrow heads indicate the extruding cell. Scale bars: 10 μm. **(E)** Proportions of apoptotic and live-cell extrusions in villus and crypt. **(F)** Lifetime distribution of 217 apoptotically and 114 live extruding cells. **(G)** Cell density around 142 extruding cells (green) and non-extruding cells from N = 5 organoids (Mann–Whitney U test on individual densities). Cell density was defined as the reciprocal of the average distance to the six nearest neighbors. Binning is for visualization only. **(H)** Average cell density of extruding and non-extruding per organoid (N = 5 organoids; two-sided one-sample Student's t-test). **(I-K)** Whole-mount stain of mouse intestinal villi. **(I)** Overview showing F-actin (phalloidin, magenta), active Myosin-II (pMyo, green) and nuclei (DAPI, blue). Scale bar: 100 μm. **(J)** Cross-section of an intestinal villus stained for pMyo (green) and nuclei (magenta). Dashed line marks the basal surface. **(K)** Zoom of villus tip in (J). **(L)** Basal Myosin-II profile along the villus (mean ± SD; N = 6 villi). **(J,K)** Scale bar: 25 μm. **(M)** Schematic: line cut reveals tension by recoil, compression by condensation. **(N)** Dissected mouse intestine stained with membrane marker (CellMask-Orange). Top: overview of villi. Bottom left: villus cross-section with magenta line marking the basal plane, shown in the bottom right. Line ablation was performed at this basal section. Scale bars: 50 μm (top), 10 μm (bottom). **(O)** Line ablation (dashed line) at the villus tip (top) and shaft (bottom). Magenta shows the basal surface before, green after ablation. Scale bars: 10 μm. **(P)** Orthogonal recoil after basal line ablation at the villus tip (left) and shaft (right). Bold lines: mean; shaded areas: S.E.M. **(Q, R)** Maximum recoil **(Q)** and initial velocity **(R)** after basal ablation at villus tip and shaft (two-sided Student's t-test). **(P-R)** Data from 12 villus tips, 7 villus shafts (N = 3 mice).

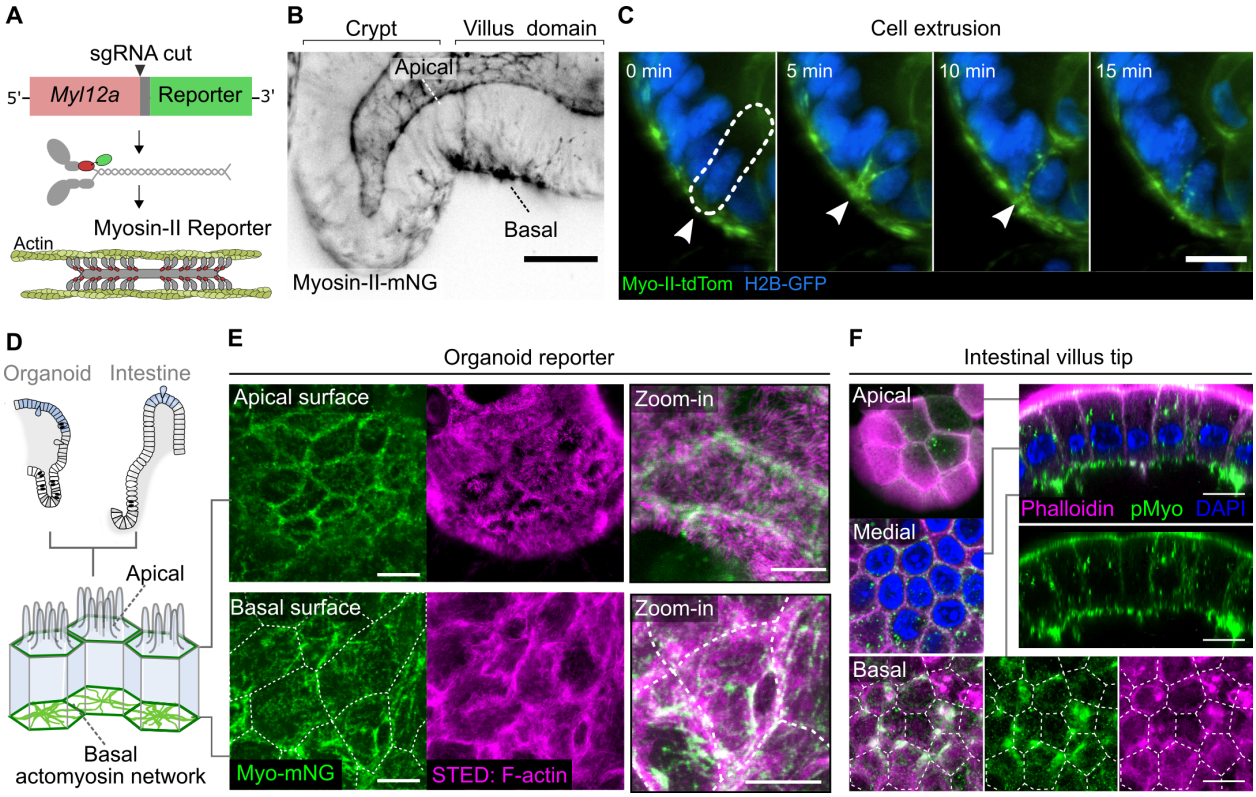
A
sgRNA cut
5'–
Myl12a
Reporter
–3'
Myosin-II Reporter
Actin
B
Crypt
Villus domain
Apical
Basal
Myosin-II-mNG
C
Cell extrusion
0 min
5 min
10 min
15 min
Myo-II-tdTom H2B-GFP
D
Organoid
Intestine
Apical
Basal
actomyosin network
E
Organoid reporter
Apical surface
Zoom-in
Basal surface
Zoom-in
Myo-mNG
STED: F-actin
F
Intestinal villus tip
Apical
Medial
Basal
Phalloidin pMyo DAPI

Fig. 2. A basal actomyosin network connects intestinal epithelial cells. (A) Generation of fluorescent reporter organoid line for Myosin-II activity. The endogenous myosin regulatory light chain gene Myl12a was tagged with a fluorescent fusion protein (mNeonGreen). **(B)** Myosin-II-mNeonGreen reporter organoid showing Myosin-II enrichment at the basal surface in the villus-like domain. **(C)** Time-lapse of an extruding cell in an organoid co-expressing Myosin-II–tdTomato (green) and H2B–GFP (blue). Dashed line marks the cell just before extrusion. Scale bar: 20 μm; imaged using light-sheet microscopy. **(D)** Schematic of cells in the villus region of intestinal organoids and in vivo villus tips (light blue). The apical surface facing the lumen features actin-rich microvilli and a cortical cytoskeleton lining the plasma membrane. **(E, F)** The basal actomyosin network (green) connects cells through junctions. **(E)** Super-resolution STED microscopy images of the apical (top row) and basal (bottom row) actomyosin network stained for F-actin (phalloidin, magenta, middle), in an organoid expressing Myosin-II-mNeonGreen (green, left). The right images show a zoom-in of a single cell with superimposed actin and myosin signals. Scale bars: 10 μm (left); 5 μm (zoom-ins). **(F)** High-resolution confocal images of cells of the mouse intestinal villus tip with top views of the apical (top), medial (middle) and basal (bottom) section and cross-sections of the entire cell (right) stained for F-actin (phalloidin, magenta), phosphorylated myosin (green) and nuclei (DAPI, blue). Scale bars: 5 μm. Dashed lines in (E, F) indicate the cell boundaries.

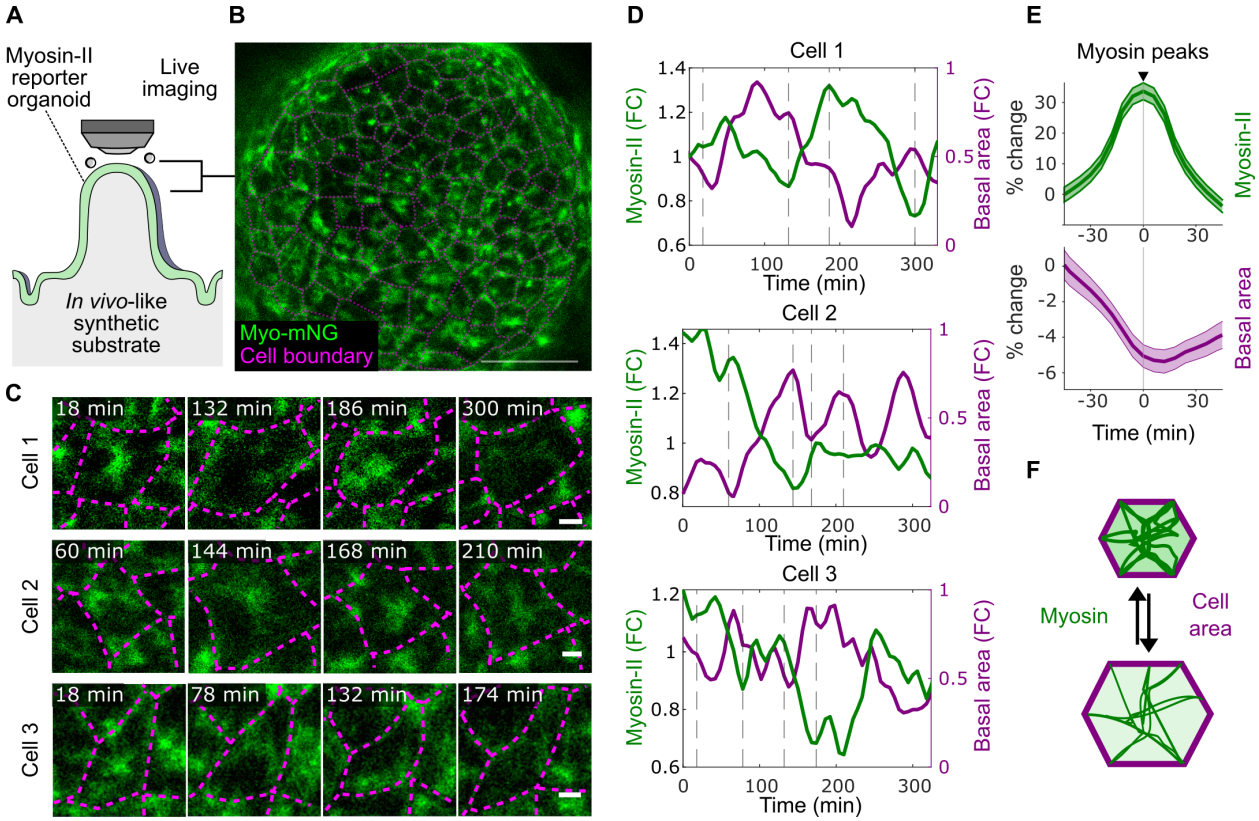
A
B
Myosin-II reporter organoid
Live imaging
In vivo-like synthetic substrate
Myo-mNG
Cell boundary
C
Cell 1
18 min
132 min
186 min
300 min
Cell 2
60 min
144 min
168 min
210 min
Cell 3
18 min
78 min
132 min
174 min
D
Cell 1
Cell 2
Cell 3
Myosin-II (FC)
Basal area (FC)
Time (min)
E
Myosin peaks
% change
Myosin-II
Basal area
Time (min)
F
Myosin
Cell area

Fig. 3. Intestinal epithelial cells use their basal cytoskeleton to exert highly dynamic pulling forces on their neighbors. (A) Experimental setup to analyze basal cell dynamics at the villus domain using crypt-villus substrates mimicking the in vivo tissue architecture. **(B, C)** The myosin reporter line co-expressing a membrane-bound mCherry fluorescent marker was grown on crypt-villus substrates and the tip region was imaged using confocal microscopy. Segmented membranes (magenta) were overlayed with the myosin signal (green). **(B)** Synthetic villus tip. Scale bar: 50 µm. **(C)** Time-lapse showing the accumulation and dissipation of Myosin-II in cells causing basal cell area pulsations. Scale bar: 5 µm. **(D)** Mean Myosin-II signal (green, left axis) and corresponding basal cell area (magenta, right axis) of three cells indicated in panel (C). Gray vertical lines indicate the respective timepoints of the micrographs in panel (C). **(E)** Time-aligned mean traces of Myosin-II peaks (top) reveals a concurrent decrease in basal cell area (bottom). Solid lines indicate mean fold change and shaded area the S.E.M. **(F)** Schematic illustrating the observed anticorrelation between basal Myosin-II and basal area.

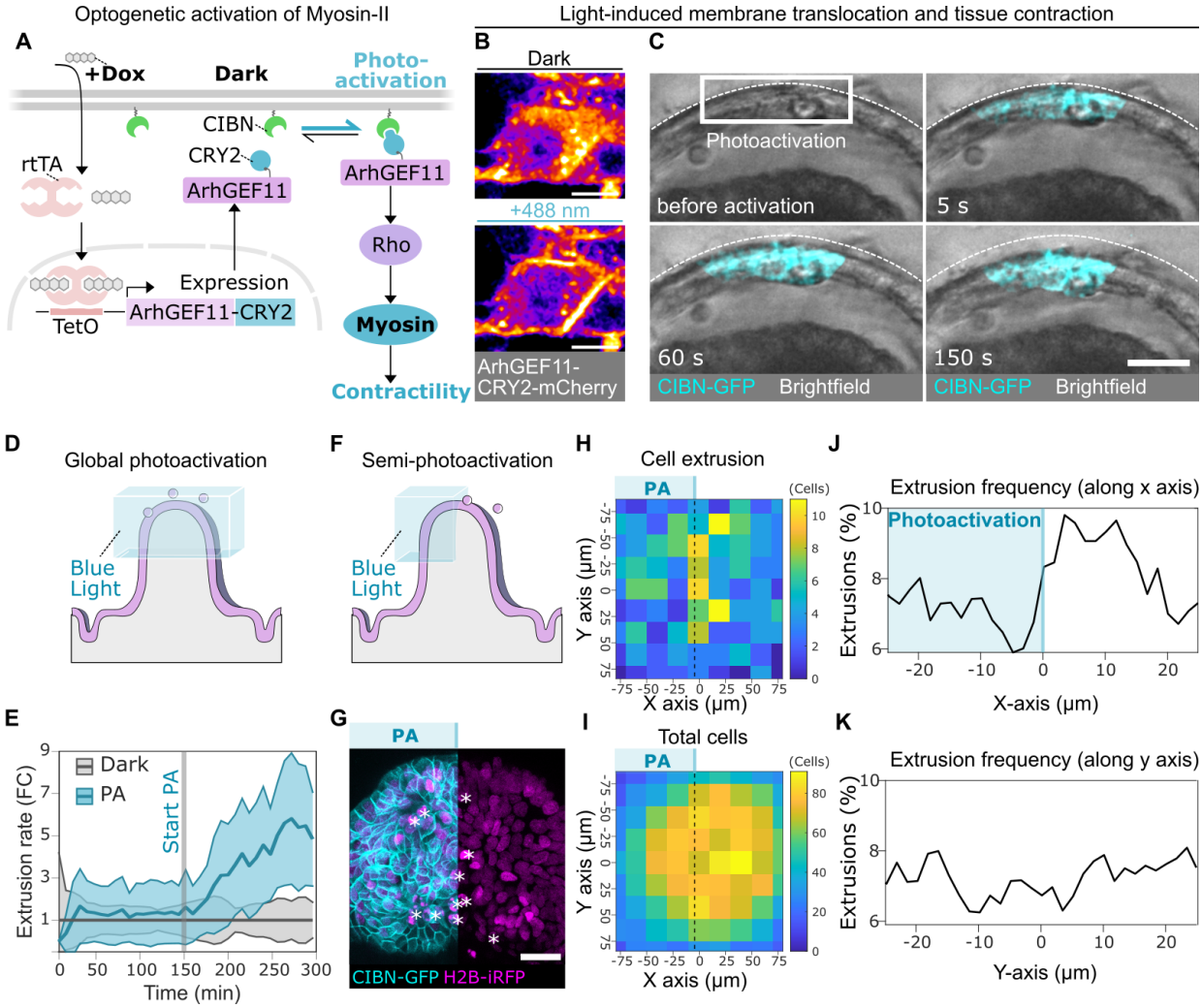
Optogenetic activation of Myosin-II
Light-induced membrane translocation and tissue contraction
A
+Dox
Dark
Photo-activation
CIBN
CRY2
ArhGEF11
rtTA
ArhGEF11
Rho
Expression
ArhGEF11-CRY2
TetO
Myosin
Contractility
B
Dark
+488 nm
ArhGEF11-CRY2-mCherry
C
Photoactivation
before activation
5 s
60 s
150 s
CIBN-GFP
Brightfield
CIBN-GFP
Brightfield
D
Global photoactivation
Blue Light
F
Semi-photoactivation
Blue Light
H
Cell extrusion
PA
(Cells)
Y axis (µm)
X axis (µm)
J
Extrusion frequency (along x axis)
Photoactivation
Extrusions (%)
X-axis (µm)
E
Dark
PA
Start PA
Extrusion rate (FC)
Time (min)
G
PA
CIBN-GFP H2B-iRFP
I
Total cells
PA
(Cells)
Y axis (µm)
X axis (µm)
K
Extrusion frequency (along y axis)
Extrusions (%)
Y-axis (µm)

Fig. 4. Differences in intercellular tension influence cell extrusion at the villus tip. (A) Schematic of the Arhgef11-CRY2 optogenetic system. Doxycycline (Dox) induces Arhgef11-CRY2 expression via rtTA (TetON). Blue light triggers its dimerization with membrane-bound CIBN, causing Arhgef11 translocation to the membrane, activation of Rho signaling, and increased myosin-driven contractility. **(B)** Arhgef11-CRY2-mCherry was recruited to the membrane upon photoactivation with 488 nm light. Scale bar: 10 μm. **(C)** A group of cells in an opto-Arhgef11 organoid was photoactivated with 488 nm light, inducing contraction. Membrane-anchored CIBN-GFP visible in the photoactivated region (blue). Scale bar: 50 μm **(D)** Setup to assess acute, global myosin activation: opto-Arhgef11 organoids on crypt–villus substrates were photoactivated at the tip (488 nm). Extrusion was tracked via H2B-iRFP. **(E)** Cell extrusion rates over time in non-photoactivated (gray) and photoactivated (blue) synthetic villi. Villi were imaged with 640 nm before 488 nm photoactivation (vertical line), which triggered up to a 5-fold increase. Rates are shown as fold change (FC) relative to dark control (mean ± standard deviation; 19 dark, 13 photoactivated villi). **(F-K)** Patterned activation of myosin-mediated tension: one half of synthetic villus tips was photoactivated (PA, blue) to create an artificial boundary between myosin-activated and non-activated cells (N = 24 villi). **(F)** Schematic illustrating the setup. **(G)** Confocal image of a villus tip with cells co-expressing opto-Arhgef11 (CIBN-GFP, cyan) and H2B-iRFP (magenta). Asterisks mark extrusion events detected within 45 min. **(H, I)** Heatmap showing the location of extrusion events detected within 2.5 h in 24 villi **(H)** and total cell density **(I)**. The dashed lines indicate the boundary of the photoactivated region (left). **(J, K)** Density of extrusion events averaged along the x-axis, with photoactivation creating a boundary between photoactivated (left, $x < 0$) and non-activated (right, $x > 0$) regions **(J)**, and along the y-dimension **(K)**. Cells near the pattern boundary extruded less in the photoactivated region and more in the adjacent non-activated region.

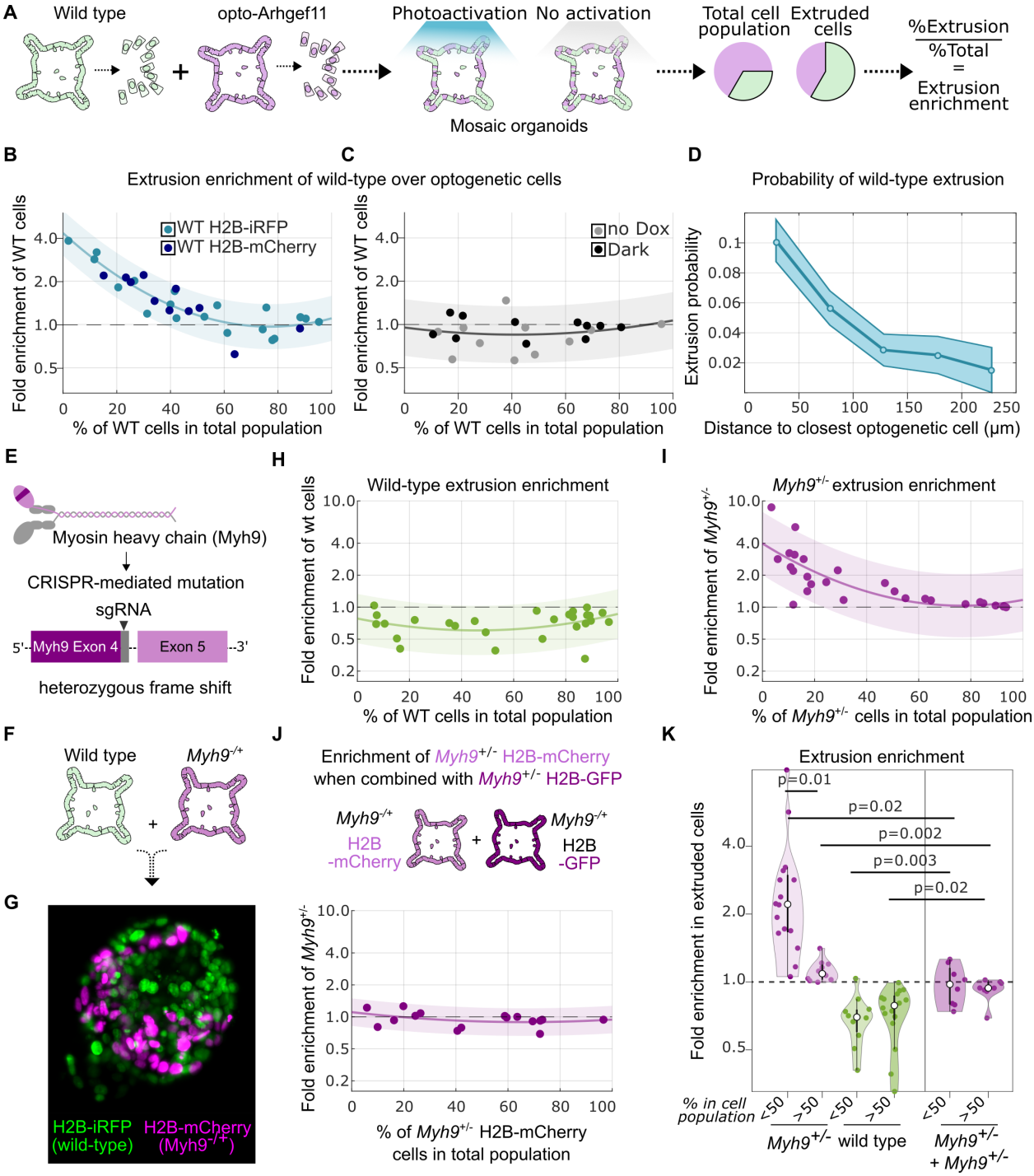
A
Wild type
opto-Arhgef11
Photoactivation
No activation
Mosaic organoids
Total cell population
Extruded cells
%Extrusion / %Total = Extrusion enrichment
B
Extrusion enrichment of wild-type over optogenetic cells
Fold enrichment of WT cells
WT H2B-iRFP
WT H2B-mCherry
% of WT cells in total population
C
Fold enrichment of WT cells
no Dox
Dark
% of WT cells in total population
D
Probability of wild-type extrusion
Extrusion probability
Distance to closest optogenetic cell (μm)
E
Myosin heavy chain (Myh9)
CRISPR-mediated mutation
sgRNA
5'-Myh9 Exon 4-Exon 5-3'
heterozygous frame shift
F
Wild type
Myh9-/+
G
H2B-iRFP (wild-type)
H2B-mCherry (Myh9-/+)
H
Wild-type extrusion enrichment
Fold enrichment of wt cells
% of WT cells in total population
I
Myh9+/- extrusion enrichment
Fold enrichment of Myh9+/-
% of Myh9+/- cells in total population
J
Enrichment of Myh9+/- H2B-mCherry when combined with Myh9+/- H2B-GFP
Myh9-/+ H2B -mCherry
Myh9-/+ H2B -GFP
Fold enrichment of Myh9+/-
% of Myh9+/- H2B-mCherry cells in total population
K
Extrusion enrichment
Fold enrichment in extruded cells
p=0.01
p=0.02
p=0.002
p=0.003
p=0.02
% in cell population
Myh9+/-
wild type
Myh9+/- + Myh9+/-

Fig. 5. Contractility differences drive competitive extrusion of Myosin-II–compromised cells in mosaic organoids. (A) Schematic of the setup: wild-type (green) and opto-Arhgef11 (purple) cells were mixed in mosaic organoids. Photoactivation increased contractility of optogenetic cells. Extrusion enrichment was defined as the ratio of a cell type's fraction in extruded cells to its fraction in the organoid. **(B, C)** Wild-type extrusion enrichment in mosaic organoids with varying wild-type fractions. Each dot: one organoid; solid line: exponential fit with 95% CI (shaded). Y-axis: log scale. Sample sizes: 31 (B), 22 (C) organoids. **(B)** Wild-type cells tagged with H2B-iRFP (light blue) or H2B-mCherry (dark blue) showed increased extrusion enrichment when in the minority. **(C)** Control conditions without doxycycline induction (no Dox) or without photoactivation (Dark) show no significant extrusion enrichment. **(D)** Wild-type cell extrusion probability increases near opto-Arhgef11 cells. Solid line: mean; shaded area: S.E.M. (82 extrusions from N = 6 organoids). **(E)** CRISPR-Cas9 strategy to generate a heterozygous loss-of-function mutant organoid line for Myh9, encoding non-muscle myosin heavy chain IIA. **(F)** *Myh9*$^{+/-}$ cells (H2B-mCherry) and wild-type cells (H2B-iRFP) were mixed as single cells to form mosaic organoids. **(G)** Light-sheet image of a mosaic organoid showing wild-type (green) and *Myh9*$^{+/-}$ (magenta) nuclei. Scale bar: 50 μm. **(H, I)** Extrusion enrichment of wild-type **(H)** and *Myh9*$^{+/-}$ **(I)** cells. Wild-type cells are underrepresented, while *Myh9*$^{+/-}$ cells are enriched among extruded cells, especially when in the minority (27 organoids). Y-axes: log scale. **(J)** Control mosaic organoids with two differentially labeled *Myh9*$^{+/-}$ populations (H2B-mCherry and H2B-GFP) show no extrusion bias (16 organoids). **(K)** Violin plot summarizing fold enrichment of *Myh9*$^{+/-}$ and wild-type cells in extruded populations, grouped by whether the genotype was in the minority (<50%) or majority (>50%) in the mosaic organoid. Each dot: one organoid. P-values: two-sided one-sample Student's t-test. Dashed line: equal extrusion probability.

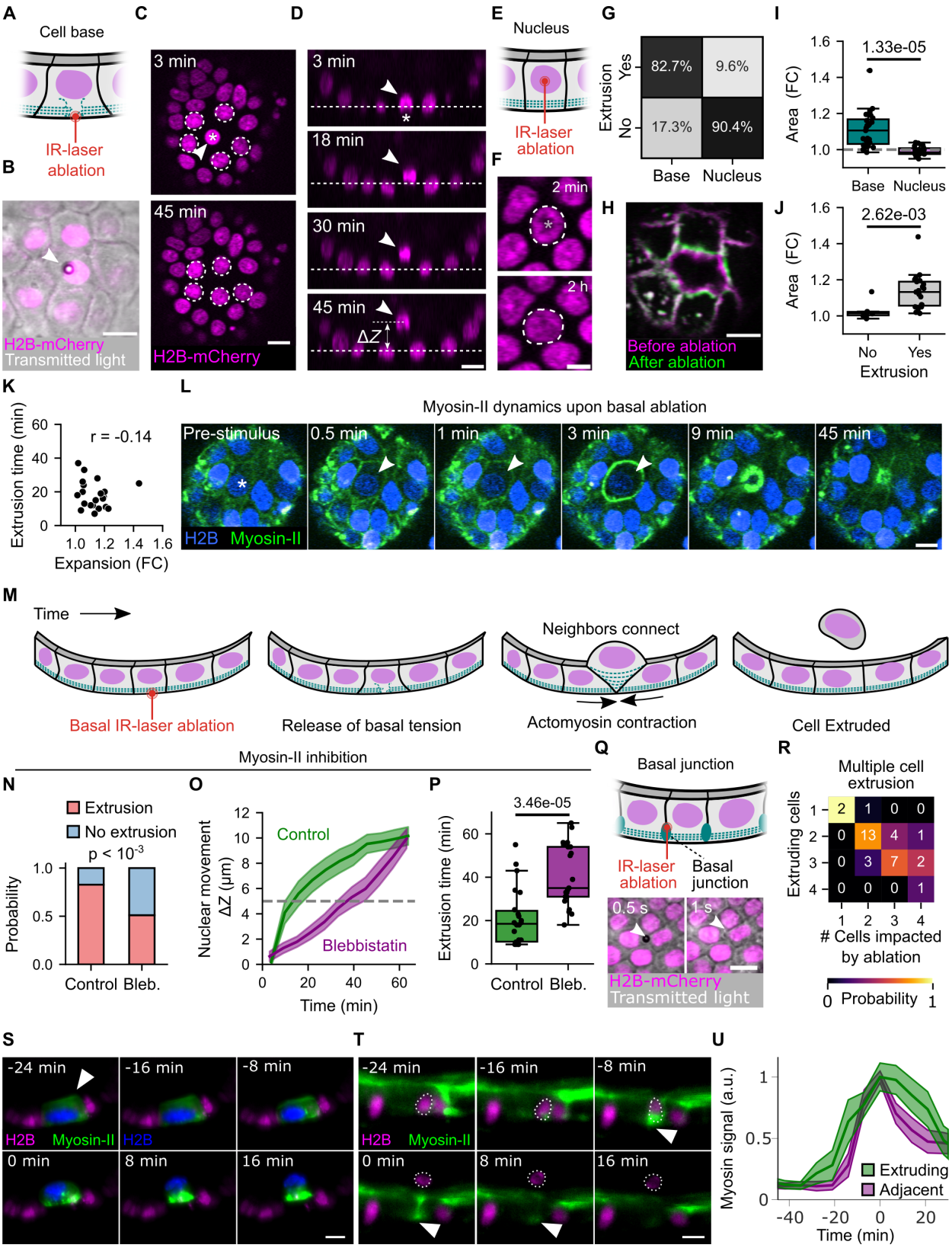
A
Cell base
IR-laser ablation
B
H2B-mCherry
Transmitted light
C
3 min
45 min
H2B-mCherry
D
3 min
18 min
30 min
45 min
ΔZ
E
Nucleus
IR-laser ablation
F
2 min
2 h
G
Extrusion
Yes
No
82.7%
9.6%
17.3%
90.4%
Base
Nucleus
H
Before ablation
After ablation
I
1.33e-05
Area (FC)
Base
Nucleus
J
2.62e-03
Area (FC)
No
Yes
Extrusion
K
Extrusion time (min)
r = -0.14
Expansion (FC)
L
Myosin-II dynamics upon basal ablation
Pre-stimulus
0.5 min
1 min
3 min
9 min
45 min
H2B
Myosin-II
M
Time
Basal IR-laser ablation
Release of basal tension
Neighbors connect
Actomyosin contraction
Cell Extruded
Myosin-II inhibition
N
Extrusion
No extrusion
p < 10-3
Probability
Control
Bleb.
O
Nuclear movement ΔZ (μm)
Control
Blebbistatin
Time (min)
P
3.46e-05
Extrusion time (min)
Control
Bleb.
Q
Basal junction
IR-laser ablation
Basal junction
0.5 s
1 s
H2B-mCherry
Transmitted light
R
Multiple cell extrusion
Extruding cells
Cells impacted by ablation
Probability
S
-24 min
-16 min
-8 min
H2B
Myosin-II
H2B
0 min
8 min
16 min
T
-24 min
-16 min
-8 min
H2B
Myosin-II
0 min
8 min
16 min
U
Myosin signal (a.u.)
Extruding
Adjacent
Time (min)

Fig. 6. Release of tissue tension triggers cell extrusion. (A-D) Point ablation of a single cell's basal surface. **(B)** Brightfield with H2B-mCherry (magenta); **(C, D)** Confocal top view (C) and cross-section (D) after basal ablation. Arrowhead indicates targeted cell; dashed circles indicate neighbors. ΔZ: vertical shift of the extruding cell relative to neighbor Z-levels. Scale bars: 10 μm. **(E, F)** Schematic **(E)** and confocal images **(F)** of point ablation in the nucleus. Timestamps in C, D, F indicate time since ablation. Asterisk indicates location of the stimulus. **(G)** Basal ablation triggered extrusion, unlike nuclear stimulation (Data from 81 basal and 94 nuclear stimulations; $p < 10^{-23}$, Fisher's exact test). **(H)** Point ablation causes cell base expansion. (magenta: before, green: after). **(I)** Cell area expanded after basal but not nuclear ablation (Student's t-test; Data from 27 basal and 18 nuclear stimulations). **(J)** Basal expansion predicted extrusion (Mann-Whitney U test; 21 extrusions, 6 non-extrusions). **(K)** Basal expansion after ablation did not correlate with extrusion time (Pearson r: -0.14). **(L)** Confocal images of Myosin-II (green) dynamics after basal point ablation. Asterisk indicates the location of the stimulus; arrowhead indicates the extruding cell. **(M)** Response to acute basal tension loss by laser-induced cytoskeletal ablation. **(N)** Blebbistatin reduced extrusion probability within 1 h after basal ablation (Fisher's exact test; 81 control, 49 blebbistatin-treated organoids). **(O)** Vertical shift (ΔZ) over time (mean ± S.E.M. of stimulated cells). **(P)** Extrusion time (Mann–Whitney U test; 22 extrusions per condition in **O**, **P**). **(Q)** Multicellular junction ablation. Arrowheads: ablation site. **(F, H, L, Q)** Scale bar: 5 μm. **(R)** Ablation of multicellular junctions triggered extrusion of nearby cells (within 9 μm; N = 34 organoids). **(S, T)** Mosaic organoids with Myosin-II reporter (green) and H2B-iRFP–only cells (magenta). Time relative to spontaneous extrusion. Scale bars: 10 μm. **(S)** Extruding myosin reporter cell autonomous upregulation of myosin. **(T)** Non-reporter cell extrusion induced myosin in neighbors. **(U)** Myosin-II levels over time in extruding cells (green) and their neighbors (magenta), aligned to extrusion. Data from 10 extruding and 15 adjacent cells.

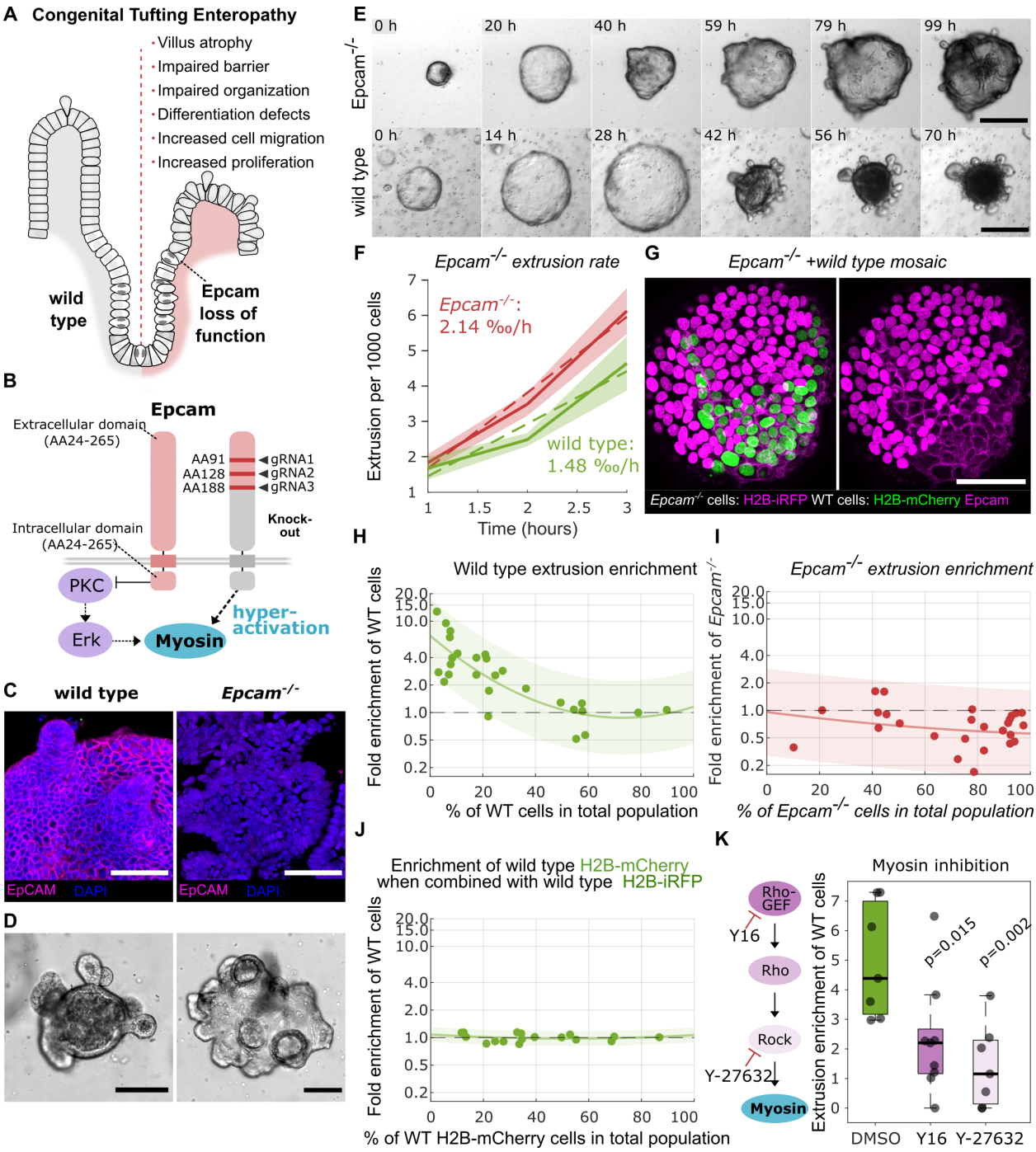
A Congenital Tufting Enteropathy
Villus atrophy
Impaired barrier
Impaired organization
Differentiation defects
Increased cell migration
Increased proliferation
wild type
Epcam loss of function
B
Epcam
Extracellular domain (AA24-265)
AA91
AA128
AA188
gRNA1
gRNA2
gRNA3
Knock-out
Intracellular domain (AA24-265)
PKC
Erk
Myosin
hyper-activation
C
wild type
Epcam-/-
EpCAM DAPI
EpCAM DAPI
D
E
Epcam-/-
0 h
20 h
40 h
59 h
79 h
99 h
wild type
0 h
14 h
28 h
42 h
56 h
70 h
F
Epcam-/- extrusion rate
Epcam-/-: 2.14 ‰/h
wild type: 1.48 ‰/h
Extrusion per 1000 cells
Time (hours)
G
Epcam-/- +wild type mosaic
Epcam-/- cells: H2B-iRFP WT cells: H2B-mCherry Epcam
H
Wild type extrusion enrichment
Fold enrichment of WT cells
% of WT cells in total population
I
Epcam-/- extrusion enrichment
Fold enrichment of Epcam-/-
% of Epcam-/- cells in total population
J
Enrichment of wild type H2B-mCherry when combined with wild type H2B-iRFP
Fold enrichment of WT cells
% of WT H2B-mCherry cells in total population
K
Rho-GEF
Y16
Rho
Rock
Y-27632
Myosin
Myosin inhibition
Extrusion enrichment of WT cells
p=0.015
p=0.002
DMSO
Y16
Y-27632

Fig. 7. Hyperactivation of Myosin-II in *Epcam*$^{-/-}$ cells disrupts epithelial homeostasis and drives competitive cell extrusion. (A) Hallmarks of congenital tufting enteropathy (CTE), a disease caused by loss-of-function mutations in *Epcam*. **(B)** Schematic of Epcam function and its role in Myosin-II inhibition. Right: CRISPR/Cas9 strategy to generate *Epcam*$^{-/-}$ organoids (guide sites shown). Epcam loss leads to Myosin-II hyperactivation. **(C, D)** Immunofluorescence staining (Epcam (magenta) and DAPI (blue)) and brightfield images of wild-type and *Epcam*$^{-/-}$ mutant organoids. Scale bars: 50 μm (C) and 100 μm (D). **(E)** Brightfield images showing growth and morphological changes of wild-type (bottom) and *Epcam*$^{-/-}$ (top) organoids over time. Scale bar: 100 μm. **(F)** Quantification of cell extrusion rates using a transwell assay and flow cytometry; *Epcam*$^{-/-}$ organoids (red) show a significantly higher extrusion rate compared to wild-type (green). Solid line shows mean and semi-transparent region the S.E.M. Data: 5 WT, 12 *Epcam*$^{-/-}$ (5 of g1 and g2; and 2 of g3) transwells **(G)** Immunofluorescence for Epcam (magenta) in a mosaic organoid with H2B-iRFP–labeled Epcam cells (also magenta) and H2B-mCherry–labeled wild-type cells (green). Scale bar: 50 μm. **(H-I)** Extrusion enrichment in mosaic organoids composed of H2B-iRFP–labeled *Epcam*$^{-/-}$ cells and H2B-mCherry–labeled wild-type cells. Extrusion enrichment of wild-type **(H)** or *Epcam*$^{-/-}$ **(I)** cells is shown at varying fractions of the respective cell population in the mosaic organoid. Wild-type cells become increasingly enriched among extruded cells as the proportion of *Epcam*$^{-/-}$ neighbors rises, while *Epcam*$^{-/-}$ cells are underrepresented (27 organoids). **(J)** Extrusion enrichment in control mosaics with wild-type cells labeled by different nuclear markers showed no bias. **(H–J)** Each dot: one organoid; exponential fit ± 95% CI (shaded). Y-axis: log scale. **(K)** Pharmacological inhibition of Rho signaling upstream of Myosin-II activity with Y16 or Y-27632 (scheme on left) reduces extrusion enrichment of WT cells in WT/*Epcam*$^{-/-}$ mosaics. Data from 7 DMSO-treated, 9 Y16-treated and 7 Y27632-treated organoids; two-sided one-sample Student's t-test.

Science
AAAS

Supplementary Materials for

Epithelial tension controls intestinal cell extrusion

Authors: Daniel Krueger†[1]*, Willem Kasper Spoelstra†[2], Dirk Jan Mastebroek[1], Rutger Kok[2], Shanie Wu[1], Mike Nikolaev[3]‡, Marie Bannier-Hélaouët[1,5]‡, Nikolche Gjorevski [3]‡, Matthias Lutolf[3]‡, Johan van Es[1], Jeroen van Zon[2]*, Sander Tans[2,4]*, Hans Clevers[1,5]*§

Corresponding authors: h.clevers@hubrecht.eu; s.tans@amolf.nl; j.v.zon@amolf.nl; d.krueger@hubrecht.eu

The PDF file includes:

Other Supplementary Materials for this manuscript include the following:

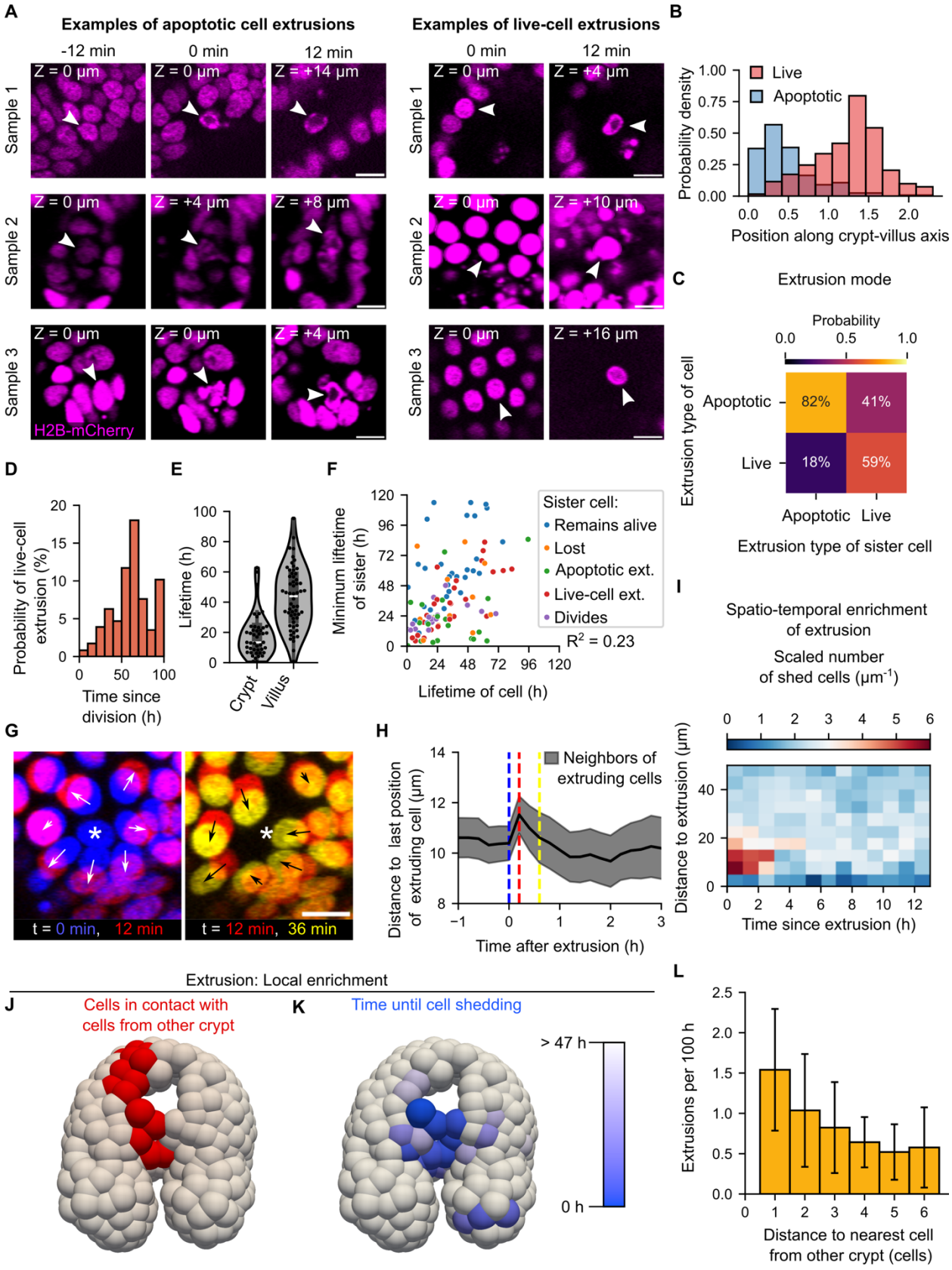
A
Examples of apoptotic cell extrusions
-12 min
0 min
12 min
Sample 1
Sample 2
Sample 3
Z = 0 µm
Z = +14 µm
Z = +4 µm
Z = +8 µm
Z = +10 µm
Z = +16 µm
H2B-mCherry
Examples of live-cell extrusions
B
Live
Apoptotic
Probability density
Position along crypt-villus axis
C
Extrusion mode
Probability
Extrusion type of cell
Apoptotic
Live
82%
41%
18%
59%
Extrusion type of sister cell
D
Probability of live-cell extrusion (%)
Time since division (h)
E
Lifetime (h)
Crypt
Villus
F
Minimum lifetime of sister (h)
Lifetime of cell (h)
Sister cell:
Remains alive
Lost
Apoptotic ext.
Live-cell ext.
Divides
R² = 0.23
G
t = 0 min, 12 min
t = 12 min, 36 min
H
Neighbors of extruding cells
Distance to last position of extruding cell (µm)
Time after extrusion (h)
I
Spatio-temporal enrichment of extrusion
Scaled number of shed cells (µm⁻¹)
Distance to extrusion (µm)
Time since extrusion (h)
Extrusion: Local enrichment
J
Cells in contact with cells from other crypt
K
Time until cell shedding
> 47 h
0 h
L
Extrusions per 100 h
Distance to nearest cell from other crypt (cells)

Fig. S1. Quantitative analysis of apoptotic and live-cell extrusions in space and time. (A) Confocal timelapse images of an organoid expressing H2B-mCherry nuclear marker showing a representative example of an apoptotic and live-cell extrusions. Note that the extruding cell's nucleus fragmented while the cell was still in the epithelium. **(B)** Probability distributions of apoptotic and live cell extrusion events along the normalized crypt-villus axis (368 live and 211 apoptotic extrusions). **(C)** Probabilities of a cell to undergo apoptotic or live-cell extrusion given that its sister either live-extruded (51 cases) or extruded apoptotically (119 cases). **(D)** Probability of a cell undergoing live-cell extrusion in the next 10 h plotted against the cell age (time since division). **(E)** Lifetime distribution for cells that undergo live-cell extrusion plotted separately for cells extruding in the crypt and the villus region. **(F)** Scatterplot showing the minimum sister cell lifetime of live-extruding cells. Colors indicate the fate of the sister cell at the last trackable time point. "Lost" indicates cells that were lost from imaging (e.g. because they moved out of view). **(G)** Movement of nuclei directly before and after cell extrusion. Scale bar: 10 μm. **(H)** Distance of neighbor cells to the last position of an extruding cell over time during an extrusion (mean ± S.E.M.; N = 15 extrusion events with 87 neighbors tracked in total). **(I)** Spatiotemporal enrichment of cell extrusion events. **(J-L)** Cells most frequently extruded in the villus domain, and most abundantly in a region where cells from neighboring crypts converged.

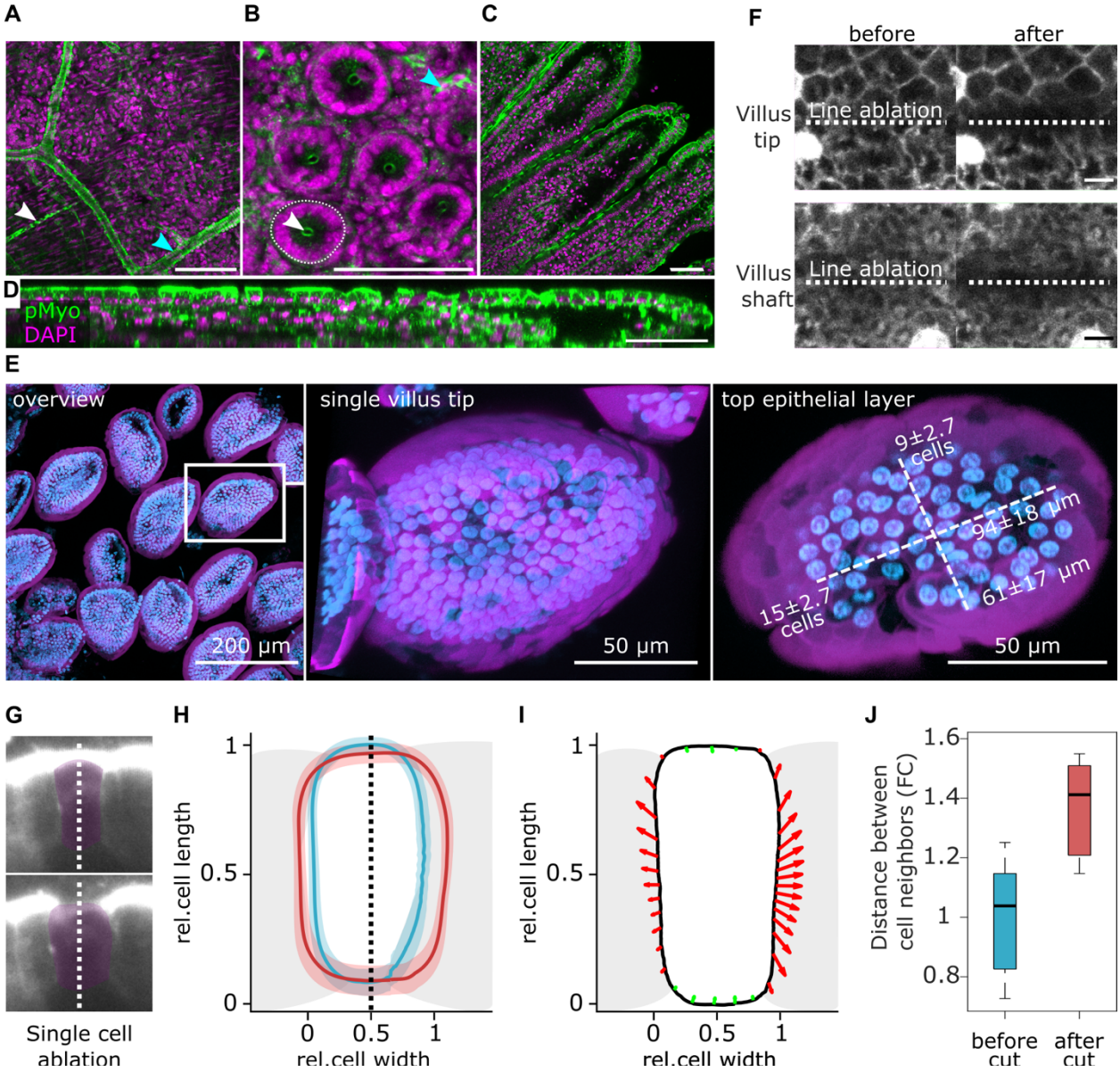
A
B
C
D
pMyo
DAPI
F
before
after
Villus tip
Line ablation
Villus shaft
Line ablation
E
overview
200 µm
single villus tip
50 µm
top epithelial layer
9±2.7 cells
94±18 µm
61±17 µm
15±2.7 cells
50 µm
G
Single cell ablation
H
rel.cell length
rel.cell width
I
rel.cell length
rel.cell width
J
Distance between cell neighbors (FC)
before cut
after cut

Fig. S2. Laser ablation reveals tensile forces at the villus tip. (A-D) Whole mount tissue stain of the mouse intestine showing phosphorylated Myosin-II (pMyo) and nuclei (DAPI). Scale bars: 50 µm. **(A)** Tissue below the intestinal crypts showing muscle (white arrowhead) and endothelia (cyan arrowhead) enriched for active myosin. **(B)** Intestinal crypts showing apical myosin enrichment (white arrowhead) and myosin signal in migratory immune cells (cyan arrowhead). The dashed line indicates the basal surface of a crypt. **(C)** Intestinal villi. **(D)** Intestinal villus positioned longitudinal to the imaging plane was imaged and quantified to obtain basal pMyo profiles. **(E)** Whole mount stain of mouse intestinal villus tips for DAPI (blue) and phalloidin (magenta) at different magnifications showing the geometry and dimensions of the villus tip. On the right: the epithelium at the villus tip. Quantification of cell numbers and dimensions based on n=15 villus tips. **(F)** Confocal section of the cell base of the villus tip (top) and villus shaft (bottom) stained with the live plasma membrane marker CellMaskOrange before (left) and after (right) line ablation (dashed line). Scale bars: 10 µm. **(G)** Still images before and after ablation of a single epithelial cell along its apical-basal axis (magenta overlay) at the villus tip. The white dashed line marks the ablation plane. Scale bar, 5 µm. **(H)** Average cell outlines before (blue) and after (red) cell ablation. Cell shapes were normalized and aligned; shaded regions indicate standard deviation across all experiments. An orthogonal recoil is observed post-ablation. **(I)** Recoil vectors (red arrows: outward retraction; green arrows: inward retraction) plotted from segmented cell outlines. Recoil occurs orthogonally to the ablation axis, consistent with the presence of tensile forces. **(J)** Quantification of the distance between neighboring cell boundaries before and after ablation shows an increase upon cutting. **(H-J)** Data from 8 ablations from N = 2 mice.

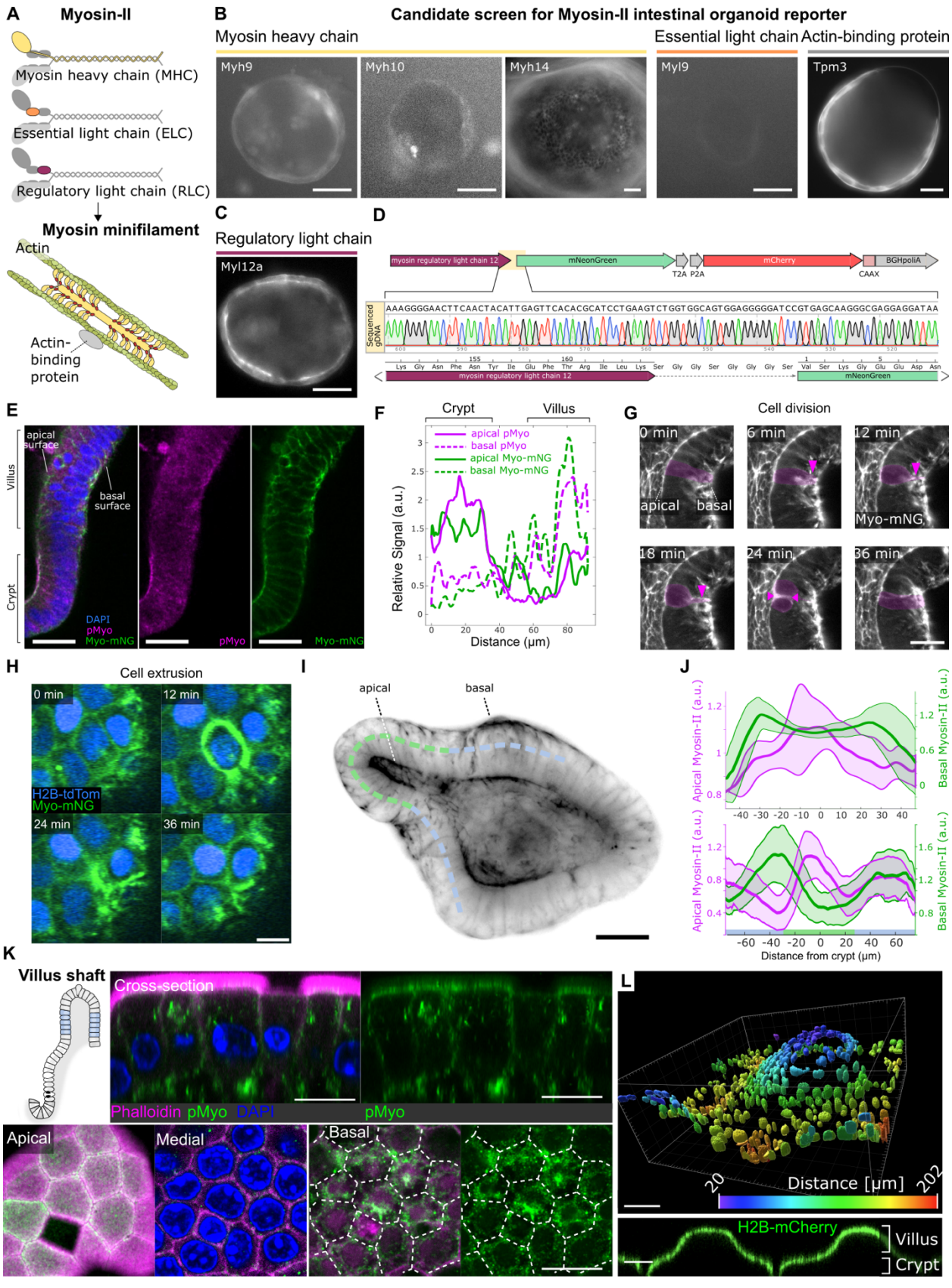
A
Myosin-II
Myosin heavy chain (MHC)
Essential light chain (ELC)
Regulatory light chain (RLC)
Myosin minifilament
Actin
Actin-binding protein
B
Candidate screen for Myosin-II intestinal organoid reporter
Myosin heavy chain
Essential light chain
Actin-binding protein
Myh9
Myh10
Myh14
Myl9
Tpm3
C
Regulatory light chain
Myl12a
D
myosin regulatory light chain 12
mNeonGreen
T2A
P2A
mCherry
CAAX
BGHpolIA
Sequenced gDNA
AAAGGGGAACTTCAACTACATTGAGTTCACACGCATCCTGAAGTCTGGTGGCAGTGGAGGGGGATCCGTGAGCAAGGGCGAGGAGGATAA
Lys Gly Asn Phe Asn Tyr Ile Glu Phe Thr Arg Ile Leu Lys Ser Gly Gly Ser Gly Gly Gly Ser Val Ser Lys Gly Glu Glu Asp Asn
myosin regulatory light chain 12
mNeonGreen
E
apical surface
basal surface
Villus
Crypt
DAPI
pMyo
Myo-mNG
F
Crypt
Villus
apical pMyo
basal pMyo
apical Myo-mNG
basal Myo-mNG
Relative Signal (a.u.)
Distance (µm)
G
Cell division
0 min
6 min
12 min
18 min
24 min
36 min
apical
basal
Myo-mNG
H
Cell extrusion
0 min
12 min
24 min
36 min
H2B-tdTom
Myo-mNG
I
apical
basal
J
Apical Myosin-II (a.u.)
Basal Myosin-II (a.u.)
Distance from crypt (µm)
K
Villus shaft
Cross-section
Phalloidin pMyo DAPI
pMyo
Apical
Medial
Basal
L
Distance [µm]
H2B-mCherry
Villus
Crypt

Fig. S3. Generation and characterization of myosin regulatory light chain reporter organoid lines. (A) Scheme of the Myosin-II multiprotein complex constituting myosin minifilaments. **(B, C)** CRISPR-HOT was used to tag components of the myosin complex with fluorescent reporters, including heavy chains (*Myh9*, *Myh10*, *Myh14*), light chains (*Myl9*, *Myl12a*), and the actin-binding protein Tpm3. Only *Myl12a* **(C)** was expressed at sufficiently high level to visualize the protein and showed expected localization pattern. **(D)** Sanger sequencing confirming in-frame insertion of mNeonGreen into the Myl12a locus (Myosin-mNG). A membrane-anchored mCherry (CAAX) was co-expressed via a T2A-P2A linker. **(E, F)** Micrographs **(E)** and quantification **(F)** of the relative signal of phospho-Myosin light chain 2 staining, Myosin-mNG. Scale bar: 50 µm. **(G)** Timelapse of Myosin-mNG reporter organoid during cell division (magenta). Arrowheads show myosin enrichments as the cell body shifting apically and during the formation of the cytokinetic furrow. Scale bar: 25 µm. **(H)** Timelapse of Myosin-mNG reporter organoid during cell extrusion. Scale bar: 5 µm. **(I)** Light-sheet section of a Myosin-mNG reporter organoid (inverted grayscale). Dashed line (crypt green, villus domain blue) indicates the profile quantified in (J). Scale bar: 25 µm. **(J)** Quantification of apical and basal myosin along the crypt-villus axes of 11 organoids (top) and of a single developing crypt over multiple time points (bottom; 50 time points with interval of 7 min); lines show mean ± SD of organoid average (top) or temporal average (bottom). **(K)** Confocal images of cells from the mouse intestinal villus shaft (blue region in schematic), showing cross-sections (top) and top views of apical, medial, and basal planes (bottom), stained for F-actin (phalloidin), phospho-myosin, and nuclei (DAPI). Dashed lines mark cell boundaries. Scale bars: 5 µm. **(L)** Z-colored 3D rendering (top) and side-view (bottom) of organoids expressing a nuclear marker (bottom) grown on synthetic substrate mimicking the in vivo architecture of the intestinal epithelium. Scale bars: 100 µm (top), 50 µm (bottom).

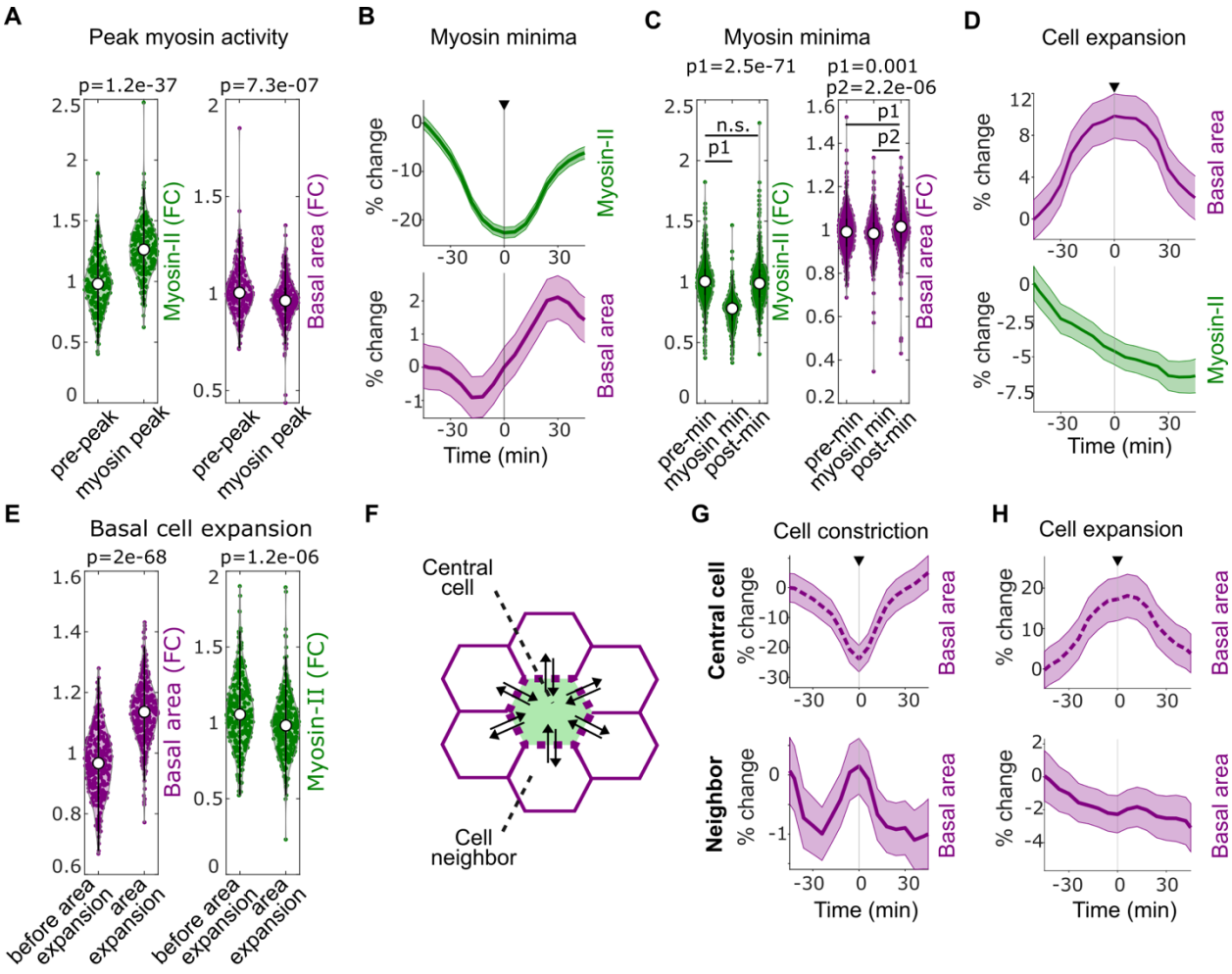
A
Peak myosin activity
p=1.2e-37
p=7.3e-07
Myosin-II (FC)
Basal area (FC)
pre-peak
myosin peak
B
Myosin minima
% change
Myosin-II
Basal area
Time (min)
C
Myosin minima
p1=2.5e-71
p1=0.001
p2=2.2e-06
n.s.
p1
p2
pre-min
myosin min
post-min
D
Cell expansion
E
Basal cell expansion
p=2e-68
p=1.2e-06
before area expansion
area expansion
F
Central cell
Cell neighbor
G
Cell constriction
Central cell
Neighbor
H
Cell expansion

Fig. S4. Dynamic Myosin-II remodeling regulates basal area fluctuations and mechanical coupling between neighboring cells. (A) Violin plots showing fold change (FC) in Myosin-II intensity and basal cell area before and during Myosin-II peaks (left), and before and during basal area expansion (right). **(B)** Time-aligned mean traces of Myosin-II minima (top) and the concurrent average change basal area (bottom) showing a concomitant area increase (mean ± S.E.M.). **(C)** Violin plots showing fold change (FC) in Myosin-II intensity (left) and basal cell area (right) before, and during and after Myosin-II minima. **(D)** Time-aligned mean traces of basal cell area expansions (top) coincide with decreasing Myosin-II levels (bottom), indicating that expansion is associated with reduced contractile activity (mean ± S.E.M.). **(E)** Violin plots showing fold change (FC) in basal area (left) and Myosin-II (right) during basal cell expansion. **(A, C, E)** White dots indicate medians; Paired comparisons: p-values from two-sided one-sample Student's t-test. **(F)** Schematic illustrating the reciprocal relationship between basal cell area (magenta) and Myosin-II intensity (green) in one cell and the physical interaction of a central cell and its neighbors. **(G)** Time-aligned mean traces of basal area for constricting cells (top; dashed line) and their neighbors (bottom; solid line). **(H)** Time-aligned mean traces of basal area for expanding cells (top; dashed line) and their neighbors (bottom; solid line). Neighboring cells contract when a central cell expands, and vice versa. Data in (G, H) shows mean ± S.E.M. Number of cells analyzed: 309 (A), 408 (B, C), 379 (D, E), 115 (G), 77 (H).

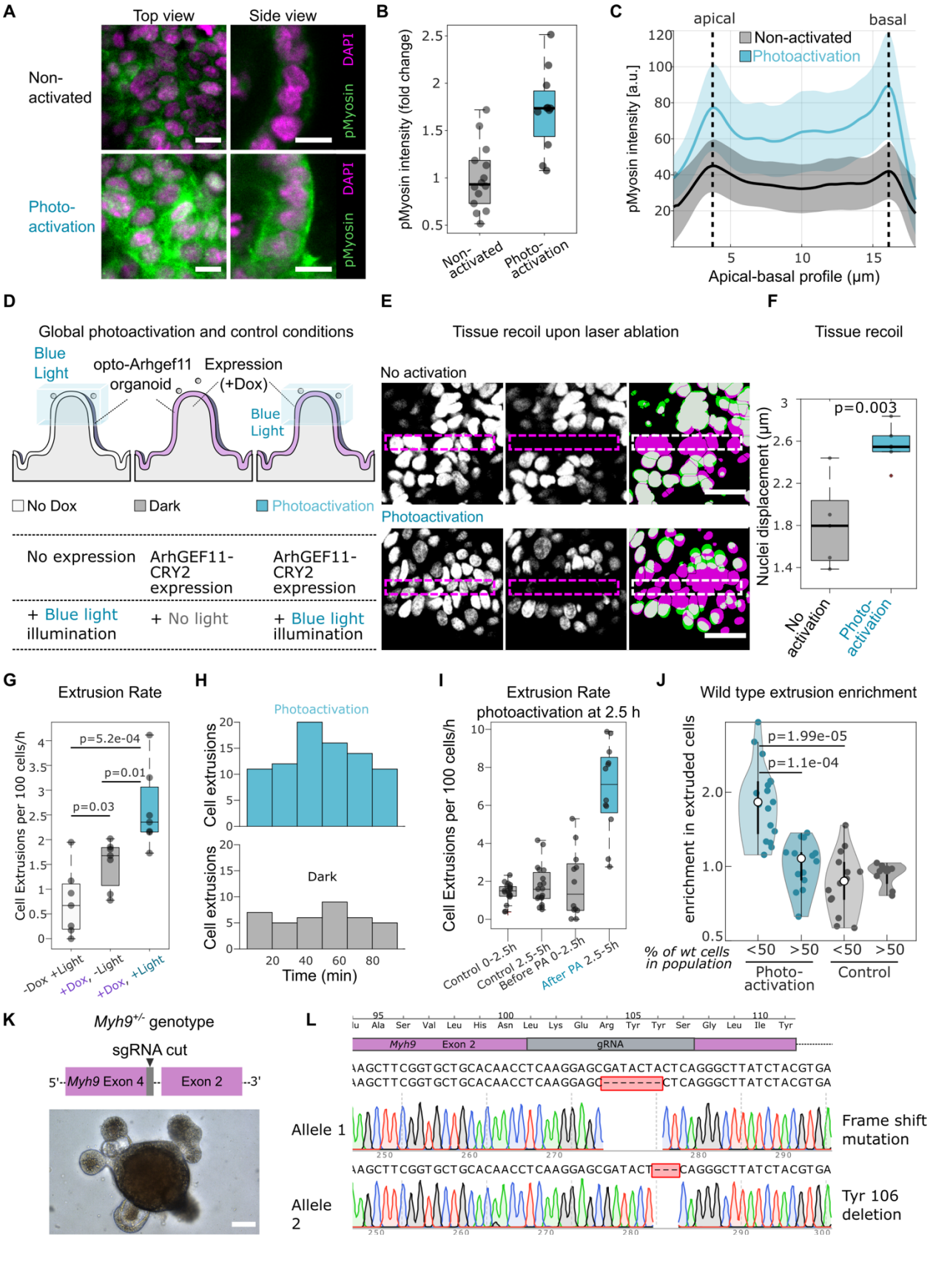
A
Top view
Side view
Non-activated
Photo-activation
DAPI
pMyosin
B
pMyosin intensity (fold change)
Non-activated
Photo-activation
C
apical
basal
Non-activated
Photoactivation
pMyosin intensity [a.u.]
Apical-basal profile (μm)
D
Global photoactivation and control conditions
Blue Light
opto-Arhgef11 organoid
Expression (+Dox)
No Dox
Dark
Photoactivation
No expression
ArhGEF11-CRY2 expression
ArhGEF11-CRY2 expression
+ Blue light illumination
+ No light
+ Blue light illumination
E
Tissue recoil upon laser ablation
No activation
Photoactivation
F
Tissue recoil
p=0.003
Nuclei displacement (μm)
No activation
Photo-activation
G
Extrusion Rate
p=5.2e-04
p=0.01
p=0.03
Cell Extrusions per 100 cells/h
-Dox +Light
+Dox, -Light
+Dox, +Light
H
Photoactivation
Dark
Cell extrusions
Time (min)
I
Extrusion Rate photoactivation at 2.5 h
Cell Extrusions per 100 cells/h
Control 0-2.5h
Control 2.5-5h
Before PA 0-2.5h
After PA 2.5-5h
J
Wild type extrusion enrichment
p=1.99e-05
p=1.1e-04
enrichment in extruded cells
% of wt cells in population
<50
>50
<50
>50
Photo-activation
Control
K
Myh9+/- genotype
sgRNA cut
5'-Myh9 Exon 4
Exon 2
-3'
L
Myh9
Exon 2
gRNA
Allele 1
Allele 2
Frame shift mutation
Tyr 106 deletion

Fig. S5. Overall increase of tissue tension increases the extrusion rate at the villus tip. (A) Confocal images of opto-Arhgef11 organoids stained for phospho-Myosin-II (green) and nuclei (magenta) under non-activated (top) and globally photoactivated (bottom) conditions. Scale bars: 10 µm. **(B)** Quantification of phospho-Myosin-II intensity in 14 control and 11 photoactivated organoids. **(C)** Apical-basal phospho-Myosin-II intensity profiles in non- and photoactivated organoids (mean ± S.E.M.; data from 7 control and 6 photoactivated organoids). Despite increased overall signal (B), subcellular distribution remains unchanged (C). **(D)** Setup: Opto-Arhgef11 organoids on crypt-villus hydrogels were photoactivated at the villus tip with (right; +Dox +Light) or without (left; -Dox +Light) prior Dox induction or imaged without blue light (middle; +Dox -Light). **(E)** Line ablation at the synthetic villus tip in non-activated or photoactivated samples. Confocal images show nuclei before (left) and after (middle) laser ablation, and as a composite (right). Scale bars: 20 µm. **(F)** Quantification of recoil based on nuclear displacement (Mann-Whitney U test, 5 villi per condition). **(G)** Extrusion rates in conditions described in (D), from 7 villi per condition. **(H)** Histogram of cumulative extrusions: photo-activated (top) and non-activated villi (bottom), 7 villi per condition. **(I)** Quantification of extrusion rates in non- (dark) and photoactivated (PA) villi. PA samples were first imaged with 640 nm light, as in controls. Data from 19 dark and 13 photoactivated villi. **(J)** Violin plot showing fold enrichment of wild-type cells in extruded populations from mosaic opto-Arhgef11 organoids, grouped by minority (<50%) or majority (>50%) presence. Data: 31 organoids; dots represent organoids; two-sided one-sample Student's t-test. **(K)** Schematic of sgRNA targeting exon 2 of *Myh9* and brightfield image of an intestinal organoid with a heterozygous knockout. Scale bar: 25 µm. **(L)** Sanger sequencing confirmed a heterozygous knockout: one allele had a frameshift causing premature truncation, the other a 3-base deletion removing Tyr106.

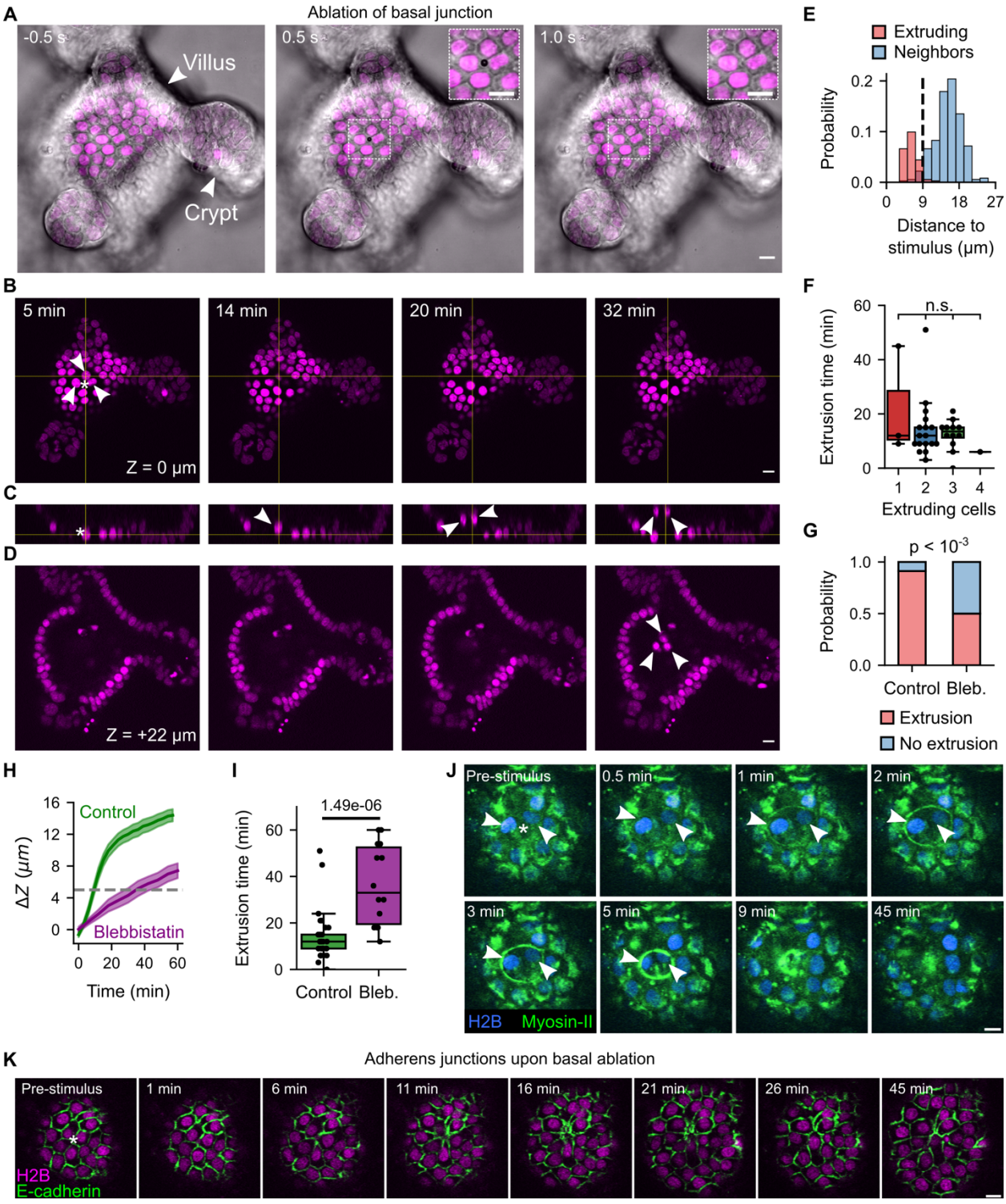
A
Ablation of basal junction
-0.5 s
0.5 s
1.0 s
Villus
Crypt
B
5 min
14 min
20 min
32 min
Z = 0 µm
C
D
Z = +22 µm
E
Extruding
Neighbors
Probability
Distance to stimulus (µm)
F
n.s.
Extrusion time (min)
Extruding cells
G
p < 10-3
Probability
Control Bleb.
Extrusion
No extrusion
H
Control
Blebbistatin
ΔZ (µm)
Time (min)
I
1.49e-06
Extrusion time (min)
Control Bleb.
J
Pre-stimulus
0.5 min
1 min
2 min
3 min
5 min
9 min
45 min
H2B
Myosin-II
K
Adherens junctions upon basal ablation
Pre-stimulus
1 min
6 min
11 min
16 min
21 min
26 min
45 min
H2B
E-cadherin

Fig. S6. Local ablation of intercellular junctions triggers multicellular extrusion. (A) Local ablation of a tri-cellular junction. Confocal images show transmitted brightfield overlayed with H2B-tdTomato nuclear marker (magenta). Dashed rectangle shows region enlarged in the zoom-in (top right). **(B-D)** Timelapse confocal images showing the extrusion of three cells induced by the ablation of a tri-cellular junction (H2B-tdTomato nuclear marker, magenta). Top view showing cells at the level of the epithelium **(B)** and shifted 22 μm towards the lumen **(D)**. The cross-section is shown in **(C)**. Arrowheads indicate the extruding cells. All scale bars in panels A-D indicate 10 μm **(E)** Upon ablation of basal junctions, cells within a range of 9 μm (measured from the nucleus center) from the ablation point extruded. **(F)** Extrusion time for cells responding to point-ablation of multicellular junction for given numbers of extruding cells. Extrusion time was independent of the number of extruding cells (n.s.: $p > 0.05$; two-sided Student's t-test; $n_1 = 3$, $n_2 = 18$, $n_3 = 12$, $n_4 = 1$). **(G)** Fraction of cases in which extrusion was observed within 1 hour after point-ablation at cell junctions, for both untreated and blebbistatin treated organoids (Fisher's exact test; 68 control and 42 blebbistatin-treated organoids). **(H)** Z position of extruding cells relative to the epithelium (ΔZ) for blebbistatin-treated and untreated controls (mean ± S.E.M.). **(I)** Extrusion time of blebbistatin-treated and untreated control organoids (two-sided Student's t-test). **(H, I)** Data from 34 control organoids and 20 blebbistatin-treated organoids. **(J)** Myosin dynamics upon ablation of basal bicellular junction. Myosin accumulated around the two affected cells (arrows), constricted and the cells extruded. Scale bar: 5 μm. **(K)** Organoid expressing a live reporter for E-cadherin (Cdh1-mNeonGreen) together with a nuclear marker (H2B-mCherry) was ablated at basal multicellular junction. The E-cadherin signal in the ablated point (asterisk) disappeared but remained present in untargeted cell boundaries suggesting that epithelial continuity was maintained during the process of multicellular extrusion. Scale bar: 10 μm.

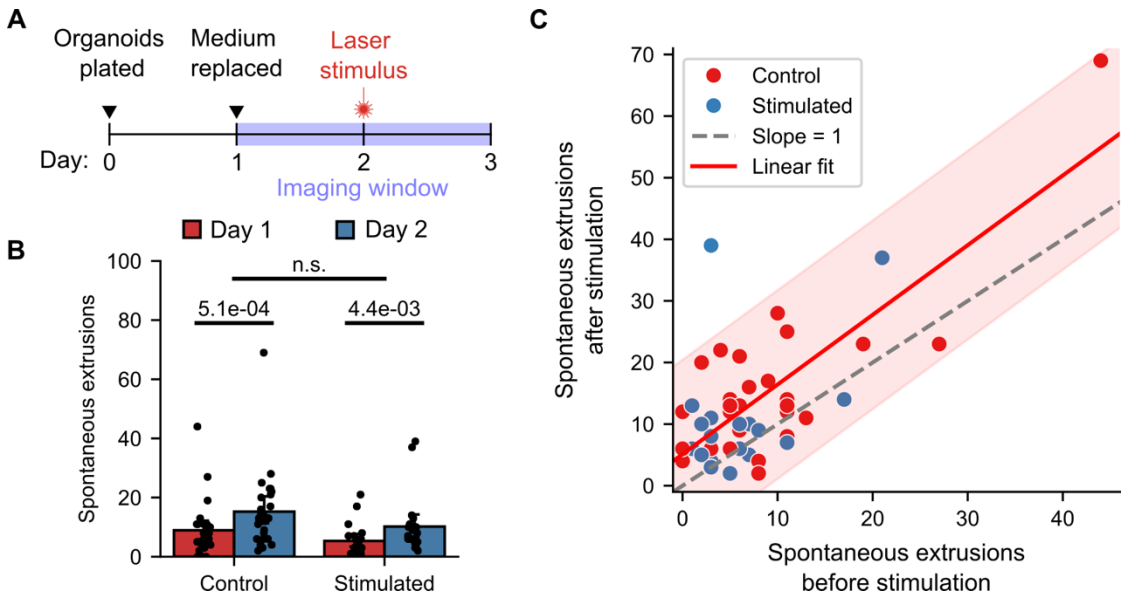

Fig. S7. Multicellular extrusion in response to basal junction ablation did not lead to an increase of overall cell death. (A) Timeline of the experiment: Organoids were plated on day 0 and organoids were imaged for exactly 24 hours, starting on day 1. After this first timelapse, some organoids were ablated at a multicellular junction in the villus (22 organoids), and the rest left as a control (28 organoids). **(B, C)** Number of spontaneous extrusions before and after stimulation. There was a significant increase in the number of spontaneous extrusions between the timelapse started on day 1 and the one started on day 2 because the organoids were older ($p < 0.01$; Wilcoxon signed rank test), but the difference in the number of extruding cells was not significantly different between control and ablated organoids (Mann-Whitney U test). Shown is the data from N = 3 independent timelapse experiments.

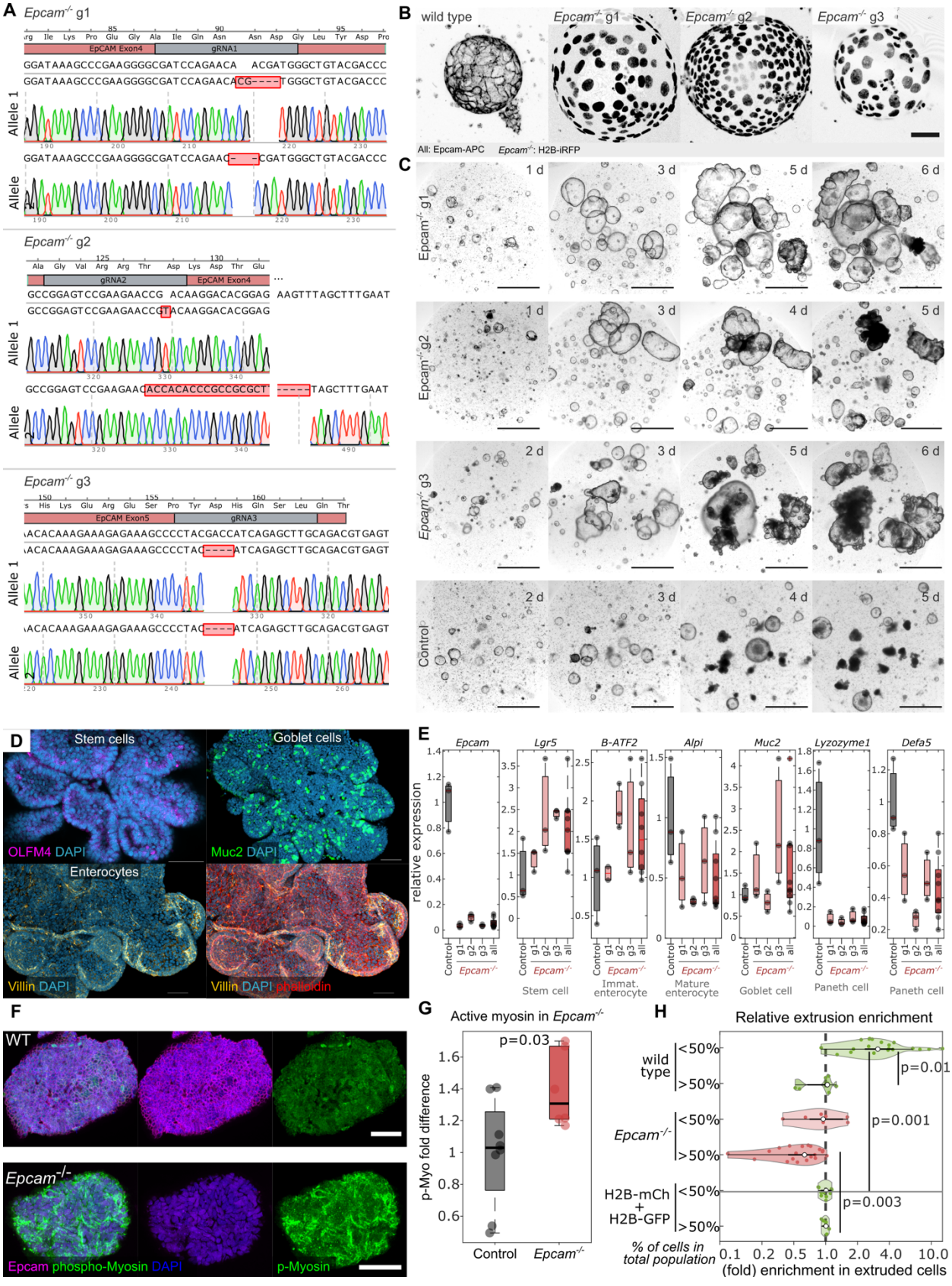
A
Epcam-/- g1
EpCAM Exon4
gRNA1
Allele 1
Allele 2
Epcam-/- g2
gRNA2
EpCAM Exon4
Epcam-/- g3
EpCAM Exon5
gRNA3
B
wild type
Epcam-/- g1
Epcam-/- g2
Epcam-/- g3
All: Epcam-APC
Epcam-/-: H2B-iRFP
C
Epcam-/- g1
Epcam-/- g2
Epcam-/- g3
Control
1 d
2 d
3 d
4 d
5 d
6 d
D
Stem cells
OLFM4 DAPI
Goblet cells
Muc2 DAPI
Enterocytes
Villin DAPI
Villin DAPI phalloidin
E
Epcam
Lgr5
B-ATF2
Alpi
Muc2
Lyzozyme1
Defa5
relative expression
Control
g1
g2
g3
all
Epcam-/-
Stem cell
Immat. enterocyte
Mature enterocyte
Goblet cell
Paneth cell
Paneth cell
F
WT
Epcam-/-
Epcam phospho-Myosin DAPI
p-Myosin
G
Active myosin in Epcam-/-
p=0.03
p-Myo fold difference
Control
Epcam-/-
H
Relative extrusion enrichment
wild type
Epcam-/-
H2B-mCh + H2B-GFP
<50%
>50%
p=0.01
p=0.001
p=0.003
% of cells in total population
0.1 0.2 0.5 1.0 2.0 4.0 10.0
(fold) enrichment in extruded cells

Fig. S8. Characterization of *Epcam*$^{-/-}$ organoid lines reveals impaired morphology, altered differentiation, and upregulated Myosin-II activity. (A) CRISPR/Cas9 gene editing of *Epcam*. Sanger traces of both alleles in three knockout clones (g1–g3) show frameshift mutations in exon 4 or 5. **(B)** Confocal images of wild-type and *Epcam*$^{-/-}$ organoids (g1–g3) expressing H2B-iRFP and both stained for Epcam-APC (both inverted greyscale), showing loss of Epcam protein. Scale bar: 25 µm. **(C)** Brightfield time course showing morphological changes in *Epcam*$^{-/-}$ organoids (g1–g3) versus wild type over 6 days. Scale bar: 250 µm. **(D)** Immunofluorescence images of *Epcam*$^{-/-}$ organoids stained for lineage markers: Olfm4 (stem cells), Muc2 (goblet cells), Villin and phalloidin (enterocytes). Scale bar: 50 µm. **(E)** qPCR analysis showing reduced expression of cell-type markers in *Epcam*$^{-/-}$ organoids. Boxplots show expression levels relative to wild type. *Epcam*$^{-/-}$ organoids expressed markers of all major intestinal lineages, indicating that differentiation still occurred. However, relative expression levels differed from control: stem cell (*Lgr5*) and immature enterocytes (*B-ATF2*) markers were elevated, goblet cell (*Muc2*) were unchanged, and mature enterocyte (*Alpi*) and Paneth cell (*Lysozyme1*, *Defa5*) markers were reduced in all three *Epcam*$^{-/-}$ lines, suggesting impaired differentiation. **(F)** Immunofluorescence staining of WT and *Epcam*$^{-/-}$ organoids for phospho-Myosin-II (green), Epcam (magenta), and nuclei (blue). Scale bar: 50 µm. **(G)** Quantification of phospho-Myosin intensity in 6 *Epcam*$^{-/-}$ and 8 wild type organoids (P-values from paired two-tailed Student's t-tests. **(H)** Violin plot showing the fold enrichment of *Epcam*$^{-/-}$ and wild-type cells in extruded populations, grouped by minority (<50%) or majority (>50%) genotype in mosaic organoids (27 organoids). The same analysis for the control (mosaic organoid with wild type H2B-mCherry and H2B-iRFP) shows no enrichment bias between differently labeled wild type cells (17 organoids). Each dot represents one organoid; p-values calculated based on two-sided one-sample Student's t-test. Dashed line indicates equal extrusion probability.

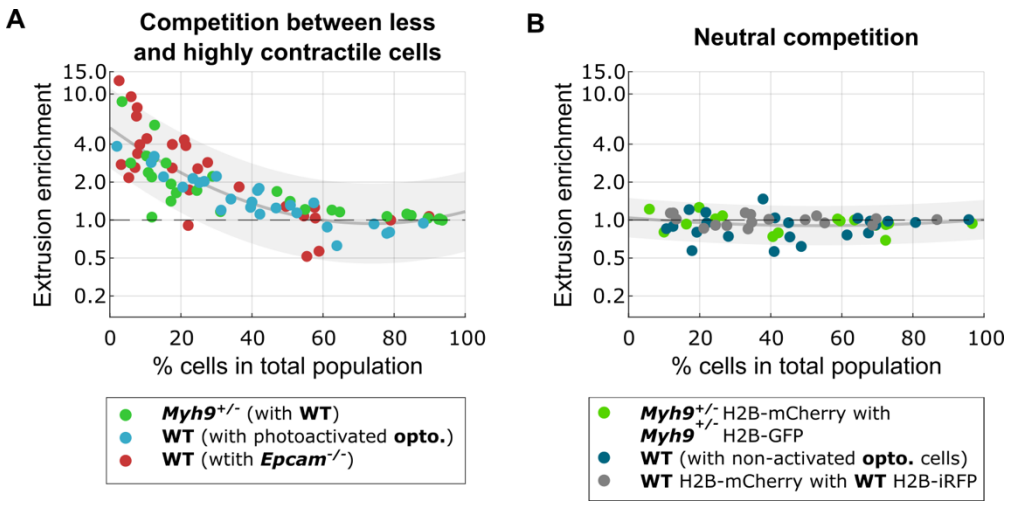

Fig. S9: Cells with lower capability to exert tension than their direct neighbors preferentially extrude across a broad range of experimental manipulations. Note that the "Enrichment" on the y-axis refers to the ratio between the fraction of cells of a type extruding and the fraction of those cells in the organoid. **(A)** Extrusion enrichment is > 1 for a cell type that is less contractile ("weaker") than the other in mosaic organoids. These are *Myh9*$^{+/-}$ cells in mosaics with wild type (WT) cells, WT cells in mosaics with photo-activated opto-Arhgef11 (opto.) cells, and WT cells in mosaics with *Epcam*$^{-/-}$ cells. Data from 28 WT/*Myh9*$^{+/-}$, 31 WT/opto. and 34 WT/*Epcam*$^{-/-}$ organoids. **(B)** Extrusion enrichment is approximately 1 (balanced) in all neutral competition conditions. These conditions are mosaic organoids consisting of *Myh9*$^{+/-}$ cells (with different nuclear markers), mosaic organoids consisting of WT and opto. cells but without photo-activation, and WT organoids from two different WT organoid lines with different nuclear markers. Data from 16 *Myh9*$^{+/-}$/ *Myh9*$^{+/-}$, 22 WT/nonactivated opto. and 17 WT/WT mosaic organoids.

Gene	sgRNA	Application
Myh9	CGATGCCAAGGCAGCTGAAT	knock-in
Myh10	ACAGCCACCCCAATCAGAAT	knock-in
Myh14	TCTAGGACAGACTGGATCAT	knock-in
Myl9	CAAACACGGCGCCAAGGACA	knock-in
Myl12a	TTCACACGCATCCTGAAGCA	knock-in
Tpm3	GGGAGGTCTACATCTCGTTC	knock-in
Cdh1	GCGGTGGTGAGGACGACTAG	knock-in
Myh9	TCAAGGAGCGATACTACTCA	knock-out
Epcam g1	GGGCGATCCAGAACAACGAT	knock-out
Epcam g2	CGGAGTCCGAAGAACCGACA	knock-out
Epcam g3	GCAAGCTCTGATGGTCGTAG	knock-out

Table S1: CRISPR-Cas9 guide RNAs.

Gene	Forward primer (5'-3')	Reverse primer (5'-3')
Actb	GGCTGTATTCCCCTCCATCG	CCAGTTGGTAACAATGCCATGT
Gapdh	GATTTGGTCGTATTGGGCGC	TTCCCGTTCTCAGCCTTGAC
Lgr5	CCTACTCGAAGACTTACCCAGT	GCATTGGGGTGAATGATAGCA
Batf2	GCCCAGCGCAGCCGGCAGAA	CCAGCTCAGTCTGCAAGGCCT
Alpi	GGCTACACACTTAGGGGGACCTCCA	AGCTTCGGTGACATTGGGCCGGTT
Muc2	GAAGCCAGATCCCGAAACCA	CCAGCTTGTGGGTGAGGTAG
Lyz1	GGTGGTGAGAGATCCCCAAG	CAGACTCCGCAGTTCCGAAT
Defa5	TCAAAAAAGCTGATATGCTATTG	AGCTGCAGCAGAATACGAAAG
Epcam	GAGTCCGAAGAACCGACAAGGA	GATGTGAACGCCTCTTGAAGCG

Table S2: RT-qPCR primers.

Movie S1. Intestinal organoids expressing a nuclear reporter allowed for cell tracking and analysis of cell extrusion. Nuclei marked with H2B-mCherry are depth-colored, with red nuclei closer to the bottom of the organoid, and blue nuclei deeper in the organoid. In the center of the white box, a cell extrudes after 22 h. Time interval: 12 min. Scale bar: 20 μm.

Movie S2. Laser ablation of the basal cell surface in dissected mouse intestine reveals that villus cells are under tension. Dissected mouse intestine was live-stained with CellMask-Orange (greyscale) to visualize the plasma membrane. The cell base in the villus tip (left) and villus shaft (right) was laser-ablated in a line pattern (dashed line). Time interval: 1 s before ablation, 5 s after ablation. Scale bars: 25 μm.

Movie S3. Cell extrusion in myosin reporter intestinal organoid. Light-sheet movie of an organoid co-expressing Myosin-II-tdTomato (green) and an H2B-GFP nuclear marker (magenta) showing an extruding cell in the cross-section. The basal surface faces the top right, the organoid lumen is in the lower left. Time interval: 6 min. Scale bars: 20 μm.

Movie S4. Myosin reporter organoids reveal polarized myosin localization pattern. Cross section of a light-sheet movie showing myosin-mNeonGreen (Fire lookup table) dynamics in an intestinal organoid with a growing crypt. Time interval: 6 min. Scale bars: 50 μm.

Movie S5. Basal myosin dynamics at synthetic villus tip. Confocal movie showing the basal myosin network and its dynamics in intestinal organoid cells grown on the synthetic villus. The first part of the movie shows the myosin reporter organoid line myosin-mNeonGreen (green) co-expressing a membrane-bound mCherry (magenta). Time interval: 12 min. Scale bars: 50 μm. The second part shows the myosin signal in an inverted greyscale color map. Segmented cells highlight an extruding cell (magenta) and its neighbors (blue). The left shows an overview of the tip region (scale bar: 50 μm), and the right a zoom-in of the extruding cell (scale bar: 20 μm). Time interval: 6 min.

Movie S6. Local photoactivation of optogenetic opto-Arhgef11 organoids. A group of cells of an opto-Arhgef11 organoid was photoactivated using 488 nm light (with box) causing a local contraction of the organoid. The optogenetic component CIBN was fused with GFP revealing its localization at the plasma membrane in the photoactivated region (green). When photoactivation was stopped, the contracted organoid tissue was able to relax. Photoactivation of a big region caused a global contraction or collapse of the organoid structure. Time interval: 10 s. Scale bars: 50 μm.

Movie S7. Point-ablation at the cell base. In this representative example, the point-ablation was targeted at the cell base, just below the nucleus of the cell in the center of the white box. Time interval: 0.5 s before ablation, 3 min after ablation. Scale bar: 20 μm.

Movie S8. Point-ablation in the nucleus. In this representative example, the point-ablation was targeted at the cell nucleus in the center of the white box. The local bleaching of the H2B-mCherry signal in the targeted nucleus shows that the ablation was successful, but the corresponding cell

does not extrude in response. Time interval: 0.5 s before ablation, 3 min after ablation. Scale bar: 20 μm.

Movie S9. Point-ablation at multicellular junction. In this representative example, a tricellular junction was targeted for point-ablation and triggers the simultaneous extrusion of the three adjacent cells in the white box. Time interval: 0.5 s before ablation, 3 min after ablation. Scale bar: 20 μm.

Movie S10. Myosin-II dynamics in extruding cell and its neighbors. In mosaic organoids Myosin-II reporter cells were mixed with wild-type cells at varying ratio. Left: An isolated single reporter cell extruding among non-reporters. Myosin-II in green, Myosin-II reporter cell co-expresses H2B-mNeonGreen (blue). Right: An isolated single non-reporter cell expressing H2B-iRFP (magenta) extrudes among Myosin-II reporter cells (green). Top: top view. Bottom: cross section. Myosin-II increased both in extruding and neighboring cells. Time interval: 8 min. Scale bar: 25 μm.

Movie S11. *Epcam*$^{-/-}$ organoids show impaired growth dynamics and inflation-deflation cycles. Brightfield time-lapse imaging of wild-type and *Epcam*$^{-/-}$ (line g3) organoids, starting 1 day after mechanical dissociation and seeding. Organoids were imaged over several days using wide-field microscopy at 37 °C and 5% CO_2. *Epcam*$^{-/-}$ organoids exhibit differences in growth with repeated inflation–deflation cycles and impaired structural development.
Time interval: 1 h. Scale bar: 200 μm.